Technical Report Documentation Page

1. Report No. ABC-UTC-2013-C3-FIU05	2. Government Accession No.	3. Recipient's Catalog No.	
4. Title and Subtitle **Principal and Considerations for Design of Small Unmanned Aerial Vehicles for Inspection and Survey**		5. Report Date April 2019 6. Performing Organization Code	
7. Author(s) Pezhman Mardanpour, https://orcid.org/0000-0002-1423-0304 Armin Mehrabi https://orcid.org/0000-0003-4736-850X		8. Performing Organization Report No. ABC-UTC-2013-C3-FIU05	
9. Performing Organization Name and Address Department of Civil and Environmental Engineering Florida International University 10555 West Flagler Street, EC 3680 Miami, FL 33174		10. Work Unit No. (TRAIS) 11. Contract or Grant No. Enter the correct number: DTRT13-G-UTC41	
12. Sponsoring Organization Name and Address Accelerated Bridge Construction University Transportation Center Florida International University 10555 W. Flagler Street, EC 3680 Miami, FL 33174		13. Type of Report and Period Covered Final report June 2017- April 2019 14. Sponsoring Agency Code	
15. Supplementary Notes Visit www.abc-utc.fiu.edu for other ABC reports.			
16. Abstract This study aims to identify the principal and considerations for the design of Small Unmanned Aerial Vehicles for inspection and survey processes. It provides a background of the current stage of the technologies and design parameters that should be taken into consideration for different aerial configurations. Additionally, a very robust design tool, Nonlinear Aeroelastic Trim and Stability of HALE (High Altitude Long Endurance) Aircraft (NATASHA) is customized to assess the aeroelastic stability and design of flexible fixed-wing that are beneficiary to survey and inspection maneuvers. Three aircraft configurations that are suitable for mapping and survey maneuvers have been designed with NATASHA. These designs are adjustable based on the payload requirement (camera, data acquisition system, etc.) and flight conditions. The computer program has been modified to take into account these parameters systematically and assess the stability of the aircraft. Moreover, an implementation demonstration of small rotorcraft drone for conceptual verification is performed for selective identified processes and applications. A model drone (rotorcraft) was used to carry out a different view of existing bridge segments in FIU Engineering Campus, which were part of the exit ramp of the Fort Lauderdale airport that was removed in 2013. As an exercise, the pilot flew the drone in the vicinity of the bridge segments and captured clear pictures of the damaged part of the bridge.			
17. Key Words Unmanned Aerial Vehicle, Drone, Bridge Construction and Rehabilitation, Inspection, Surveillance and Mapping, Aeroelastic Stability, NATASHA.		18. Distribution Statement No restrictions.	
19. Security Classification Unclassified.	20. Security Classification Unclassified.	21. No. of Pages 55	22. Price

Form DOT F 1700.7 (8-72) Reproduction of completed page authorized

(this page is intentionally left blank)

Principal and Consideration for Design of Small Unmanned Aerial Vehicles for Inspection and Survey

Final Report

April 2019

Principal Investigator: Dr. Pezhman Mardanpour

Department of Mechanical and Material Engineering
Florida International University

Authors
Pezhman Mardanpour
Armin Mehrabi

Sponsored by
Accelerated Bridge Construction University Transportation Center

A report from

Mechanical and Materials Engineering Department
FIU College of Engineering and Computing
10555 West Flagler Street
Miami, FL 33174

Tel: 305-348-2522
https://mme.fiu.edu/

DISCLAIMER

CONTENTS

LIST OF FIGURES

LIST OF TABLES

ACKNOWLEDGMENTS

This project was supported by the Accelerated Bridge Construction University Transportation Center (ABC-UTC at www.abc-utc.fiu.edu) at Florida International University (FIU), as the lead institution, and Iowa State University (ISU) and the University of Nevada-Reno (UNR) as partner institutions. The authors would like to acknowledge ABC-UTC support.

The author would like to extend special appreciation to the ABC-UTC and the U.S. Department of Transportation Office of the Assistant Secretary for Research and Technology for funding this project.

The author would like to thank all the State DOTs that participated in the survey; this work would not have been possible without their participation.

The author would like to thank the Research Advisory Panel members: Drs. Sakhrat Khizroev, and Ibrahim Tansel

CHAPTER 1:INTRODUCTION

1.1. Project Motivation

In recent years, drone technology has emerged in many industries and applications, greatly impacting and revolutionizing their processes. They have broad ranges of application from governmental, to civil, military and many more applications. The use of drone in the construction industry has ranged from construction management to inspection and evaluation of constructed facilities. It is therefore believed that drone technology has also a place in bridge construction, especially when geometry control, inspection, and surveying/mapping is concerned.

This study is designed to investigate the applications within the bridge construction and rehabilitation where drone technology can be utilized for improving or facilitating the process for accuracy, economy, timeliness, and safety.

1.2. Research objectives

The objectives of this research were to identify processes in bridge construction and rehabilitation that can benefit from drone application, and development of preliminary drone systems and design parameters that would best serve these processes. A comprehensive literature review for the current stage technology and limitations that cause complication in drone usage for this application as well as the solutions to these limitations are provided. The study also provides design requirements; identifies the existing drone systems that readily are applicable and those that would require adaptation or new designs. An example of implementation for the purpose of demonstration was performed for selective identified process and application. The objectives can be categorized as follow:

- *Objective 1 – Identification of bridge Construction processes benefiting from drone application*: A review of available literature and data was performed to study various processes and operations carried out for both new construction and rehabilitation of existing construction. These processes were categorized based on how they would benefit from drone application.
- *Objective 2 – Determination of drone design parameters and technology for bridge construction processes*: Available drone technologies are reviewed within bridge construction and other industries, and general applications benefiting the bridge construction industry. Also, the most important design parameters are identified.
- *Objective 3 – Small Unmanned Aircraft Design and Aeroelastic Trim and Stability*: The Nonlinear Aeroelastic Trim and Stability of Hale Aircraft (NATASHA) which is the state-of-the-art computer program for analysis of different fixed-wing UAV configurations is presented. NATASHA was developed primarily under NASA grant at Georgia Institute of Technology. The design input variables of NATASHA for the purpose of customization of different UAV for DOT engineers are explained. Three main aircraft configuration examples are provided. These inputs are customized for DOT engineers to be able to design the aircraft while satisfying stability concerns. Furthermore, two different rotorcrafts were used to first, model a sensor mounted on the drone and shows the asymmetric loading state and second, to obtain pictures carry out different views of the existing bridge segments in FIU Engineering Campus.

1.3. Research Advisory Panel (RAP)

The project work and the developed survey were done in collaboration with the Research Advisory Panel (RAP). The following people participated in the RAP:

- Prof. Ibrahim Tansel
- Prof. Sakhrat Khizroev

1.4. Report Overview

The overall approach of this project will be organized in three basic stages; search of background information for identification of processes within bridge construction and rehabilitation where drone application would be beneficial, and identifying appropriate drone systems and design parameters, and finally providing a numerical analysis tool and verification of the existing drone configurations through experimental trials within the scope and budget limitation.

CHAPTER 2. IDENTIFICATION OF BRIDGE CONSTRUCTION PROCESSES BENEFITING FROM DRONE APPLICATION

In recent years, drone technology has entered many industries and applications, greatly impacting and revolutionizing their processes [1-6]. It is strongly believed that drone technology has also an important role to play in bridge construction and rehabilitation, especially when geometry control, inspection, and surveying/mapping are concerned.

Application of drone not only directly reduces the effort for surveying and mapping [7-8], it also lowers the cost of design, construction, and rehabilitation processes that rely heavily on inspection and surveying [9]. This, in turn, will help to eliminate many potentials for major errors and misfits during the operation, and increasing the safety.

2.1. Construction management

The potential applications of UASs for construction tasks will be further discussed in this section, referencing a study conducted by Irizarry and Costa [10]. A collection of 200 photos and videos were gathered from test flights performed at three locations in the U.S. and Brazil. A UAS, DJI Phantom 2 Vison+, was used and was selected due to its easy-to-use control system and low-cost. It was most similar to what construction workers would be used on sites. Results were quantified through interviews of the users of the system and the benefits and usefulness were assessed.

The results showed that there is a lot of potential for applications in this field including monitoring of project progress and safety conditions, evaluation of job sites logistic plans and inspections. The results also shone a light on the issues that could surface with the use of the UASs. The projects studied revealed that workers would stop working as they would see the drones fly by. To avoid this situation training and communication with employees regarding the use of the UASs on site can be implemented. Flight safety and potential hazards caused by these distractions or control/malfunctions need to be further evaluated. A systematic and standardized approach to the use of UASs on site is required to address issues on mission planning and safe flight conditions. Further research is being conducted on how to finalize these plans and ensure the safety of all personnel working on the construction site.

There were new applications, problems, and opportunities for UASs that came along with this project that were not initially projected or discussed. For example, project personnel wanted to use the images collected to help with training, documentation, and marketing since it provided different perspectives and information about their job site, equipment, building processes, and neighboring areas affected by the construction. Additionally, to standard aerial photography, the visual assets could give more control of what they wanted to be documented.

A cost analysis showed that obtaining authorization to be able to fly while still meeting requirements would increase the expenses involved in using UASs on construction sites. However, these costs are expected to decrease when permanent regulations are placed on the usage of UAS around 2017. Overall the benefits gained by using UAS for project management are apparent but more quantified results are necessary to clearly demonstrate the impact to this field. As UAS become more popular and used consistently, more data will be available to study the financial implications and direct benefits of employing these systems. With the research gathered thus far, there is clear potential for applications of drones in construction since companies can invest in one project and then modify to use on several other projects incurring little additional costs.

2.2. Survey and mapping

Drones can capture data to be used in a variety of applications for surveying and mapping. McNiel and Snow [7] discussed different methods of surveying and mapping. The first method was the Automated mapping. In this method control points must be established either by ground features with known coordinates or markers placed at locations around the area that will be mapped. These control points will establish the scale (map distance to the real-world distance), feature height, and north orientation. The drone's flight path is calculated using a mission planning application which enables autonomous flying. It will fly at a set altitude while taking pictures at 2 or 3 seconds intervals where each image should overlap the previous one by 80% to the front and 60% to the side. Most data are accessed from the drone after the mission, however; some mission planners enable data to be streamed during the flight to the operator. Different GIS software applications can then process the images taken into maps.

The second method discussed in the work by McNiel and Snow [7] was Cadastral surveying. This method establishes boundaries for properties including buildings and land. In most cases, only licensed land surveyors can conduct this survey for the use of selling, buying and renting a property. These surveys are able to describe (1) the size of the property, (2) the location of buildings, fences and driveways, (3) potential intrusion locations, and (4) utility easements (legal rights to use another's land for a specific purpose). The images gathered by drones can be used to create Orthomosaic maps (highly detailed overlapping images of a defined area, true to scale). This can help identify bounders and land features and in turn create 2D maps. The acquisition cost of data using this method is very inexpensive which can have a major impact on the real estate and appraisal markets.

McNiel and Snow [7] also explained Corridor surveying. Drones in this method can provide a cost-effective alternative of collecting data suited for mapping road, highway, and railway infrastructures. Images captured by drones can render photomosaic images of pavement, lane marking, and general road conditions. It can also provide a digital surface model (DSM). A Mexican surveying company, SkyLab, was able to successfully map 620 miles of highways for a government agency with the help of DroneDeploy.

The volumetric calculation was another method reported by McNiel and Snow [7]. Mining and construction sites need to measure the volume of material extraction pits and stockpiles frequently. Drones can accomplish this because once images are mapped, DSMs can be created, and ground features can be measured from there. If traditional mapping methods were used to calculate these volumes, a ground-based surveyor would have to measure every 5 or 10 feet, which would be time consuming and dangerous as well as generating few reference points. A DSM, on the other hand, will have more reference points and will take less time to cover a larger site. For example, Dallas VanZanten, owner of SkyMedia Northwest, said his DJI Phantom 3 drone covered the 30-acre site in 30 minutes in comparison the original method that would take a whole day of collection. Once the DSM is created, polygons are drawn around each stockpile and the volume is calculated.

McNiel and Snow [7] also presented the LiDAR mapping method. LiDAR captures minute details that photos cannot. With these details mapping and surveying professionals can create digital representations of objects, the ground, and buildings. LiDAR is based on RADAR using laser light instead of radio waves. Laser beams are sent out in all directions and reflected energy is collected then high-speed computer processing is performed and a scanner can create a virtual map of the area. Most LiDAR units are heavy and required to be mounted on trucks or manned aircraft. For

the past couple of years, manufacturers such as Riegl, Routescene, and Velodyne have come up with a way to reduce the weight and size of the units. Now it is possible to mount them on large drones. By using drone-mounted LiDAR systems, vision cameras, GPS and advanced computer processing, it is now possible to remotely pilot a flying LiDAR scanner. This solution costs significantly less than vehicle-based mobile systems and LiDAR is a better technology compared to the similarly inexpensive method of photogrammetry. LiDAR has technology that can assess strong shadows, areas of poor contrast or featureless surfaces, unlike photogrammetry. Photogrammetry also requires access to the site to survey ground control points. LiDAR eliminates this time-consuming task.

Moser et al. [8] suggested that survey data plays a very important role as a starting point for the development of the design of roads and construction, and accuracy and precision of survey data is essential for project-to-field data transferring. They analyzed two commonly used methods, GPS and total station as well as the new technology of the unmanned aerial system. They found that GPS Real-Time Kinematic (RTK) and GPS COPOS methods present similar deviations from the total station results. However, GPS RTK demonstrates more reliable results while UAS methods resulted in even higher deviations compared to total station making UAS the least accurate method. Although there was a loss of accuracy, using UAS was reported to be relatively inexpensive and a fast surveying method.

2.3. Inspection

A comprehensive study done by Zink and Lovelace [9] founded that drone inspections of bridges would decrease the time, money, and interruption needed to inspect a bridge. This is important because it is estimated that there are 300,000 bridges in the United States alone that need an inspection. Metni and Hamel [11] discussed the benefits of the bridge inspection using a UAV as decreasing the accidents during the inspection, reduction in the required working hours and heavy logistics which results in the reduction of the required budget, and provides the possibility to have the bridge open to traffic during the inspection. Yang et al. [12] found that using a drone for bridge inspection would only require three operators which is fewer than the number currently required. It also costs less to use a drone rather than using large special equipment or setting up scaffolding. Figure 1 shows the advantageous of the drone in bridge inspection.

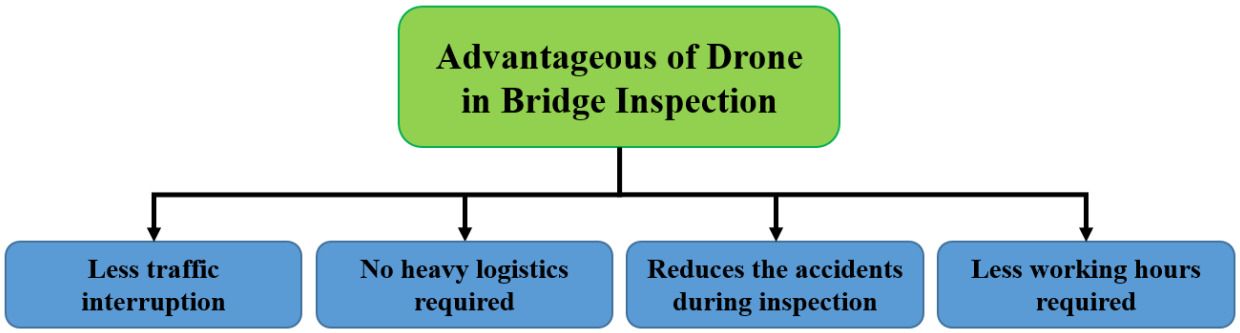

Figure 1: Advantageous of the drone in bridge inspection

2.3.1. Alternative to conventional inspection (visual inspection)

Citir et al. [13] suggested visual inspection as a useful initial step to identify potential anomalies or damage from salient features in the inspection process. During the visual inspection, the

geometric characteristic of a component is investigated along with any existing leaks, alignment of connections and more. This method can be categorized as direct, remote or translucent visual testing. The visual inspection process can use existing technologies to enhance the process. The use of optical instruments such as magnifying glasses and illuminated magnifiers as well as computer-assisted viewing systems can improve the visual analysis. Charge-coupled device and borescopes can also be used. Specialized inspections can use certain tests like liquid penetrant tests and magnetic particle tests to provide more data to observe defects. Light detection and ranging (LIDAR) allow for greater resolution in imaging. LIDAR can be used for geospatial imaging by using lasers to create 3D representations. The imagery created can be inspected visually for material geometries and location analysis.

Visual inspection methods are economical, simple and fast compared with another non-destructive testing (NDT) that require more expensive equipment. Visual inspection in comparison to other NDT methods does not require extensive training and it can be applied in any type of materials and geometries. One downside is that visual inspection can only identify surface discontinuities and defects visible on the surface can be difficult to quantify. Other NDT methods may be additionally used to confirm the accuracy of measurements and detection collected from visual inspection [13].

2.3.2. Non-Destructive Testing (NDT) for health monitoring and damage detection

Farhangdoust et al. [14] reported and evaluated different non-destructive testing (NDT) methods to assess the components of bridges built using Accelerated Bridge Construction (ABC) method, including the closure joints and bridge deck, and characterize different deteriorations, defects, and damages. They suggested that in order to choose the method, one must decide which technology is most reliable and repeatable as well as which one will provide better accuracy and easier interpretation. They conducted a comprehensive literature review on NDT methods for field inspection and damage detection and they categorized these methods as follows:

- Impact Echo Testing (IE)
- Microwave Testing (MW) – Ground Penetrating Radar (GPR)
- Sonic Pulse Velocity Testing (SPV)
- Ultrasonic Testing (UT)
- Phased Array Ultrasonic Testing (PAU)
- Infrared Thermography Testing (IR)
- Acoustic Emission Testing (AE)
- Impulse Response Testing (IRT)
- Laser Testing Method (LT)
- Radiographic Testing (RT)
- Magnetic Flux Leakage Testing (MFL)
- Visual Testing (VT)
- Global Structural Response Testing (GSR)
- Chemical and Electrical Testing (CET)

They categorized these methods based on their suitability for the most common defects that may occur in deck closure joints such as delamination, cracks, voids, and corrosion. Based on their

finding, GPR is the most applicable method to detect delamination, voids, and corrosion, and UT is the most applicable method to detect cracks [14].

2.4. 3-D scanning and simulation for checking tolerances for installation of new elements on site.

Previously, due to the lack of detailed monitoring of the geometries of prefabricated components and their spatial relationships, various misalignments have occurred at their connections. Oftentimes there are many trades in the manufacturing and installation of these components and therefore, it is a challenge to capture and analyze these geometries. During transportation and construction, further complications can arise for tolerance checking, since it is difficult to check for constructability issues. Conventional surveying methods cannot capture detailed geometries, including camber, sweep, and twists, needed to analyze important components within the allocated time constraint. By the time engineers can realize this misalignment it is usually too late in the process. Manual modeling can also be tedious and not suitable for frequent assessments. They will fail when the components undergo large deformations caused by concrete shrinkage and other reasons [15].

The development of 3D imaging systems, computer vision, and tolerance networks can provide detailed, frequent and proactive tolerance control of these components. Two challenges remain for these technologies. The data collection challenge is to determine how to ensure fast and comprehensive 3D data collection within the time constraints in the applicable workplaces. Sometimes when collecting data time can be spent unnecessarily on collection high-resolution data for flat and straight geometries, or important details can be missed when analyzing large quantities of data. The data processing challenge is the issue with deriving information of the components from the 3D data collected in the most efficient and reliable way. The most state-of-the-art processing tools still require users to conduct a large amount of manual processing and interpretation of information of objects like dimensional errors [15].

Kalasapudi et al. [15] developed a computational framework for more efficient and effective tolerance analysis of prefabricated components using 3D imaging technologies. Data of pre-fabricated components collected by laser scanners and 3D imaging technologies can help adjust the data locations and imaging parameters to their geometric complexities. Detailed data collection focused on objects that have high curvature and roughness. Based on high-quality 3D imagery data a tolerance network was generated through propagations of fabrication and installation errors – known as building information models. Spatial pattern analysis enabled automatic derivation of the tolerance network to support an automated tolerance checking. This can reduce the time data is collected while also ensuring there is a high data density for the tolerance checking. The integration of 3D imaging mechanisms and spatial pattern analysis methods were examined to demonstrate how they enable detailed tolerance analysis while reducing the time needed for the data collection and analysis.

CHAPTER 3. DETERMINATION OF DRONE DESIGN PARAMETERS AND TECHNOLOGY FOR BRIDGE CONSTRUCTION PROCESSES

3.1. History of Unmanned Aircraft Systems

There are many system types and missions in the field of Unmanned Aircraft Systems (UASs). Although long-endurance, mid-altitude range UASs, like the Predator, is the most widely known due to their contributions in the recent conflicts in Iraq and Afghanistan, there are other UAS systems that are hand-launched like the Raven. There are many perceptions of UASs. Whether some may see them as sophisticated model airplanes or aircraft without pilots, these perceptions do not fully grasp the complexity, diversity and full capabilities these systems have. In this section, detailed features and attributes of UASs will be discussed along with the history to demonstrate how these systems have adapted over time [16].

To define UAS, the unmanned system must include a flying vehicle. Unmanned aircraft have also taken on different names including drone, remotely piloted vehicle or aircraft (RPV or RPA), unmanned aerial vehicle (UAV), organic aerial vehicle (OAV), aerial robotics, micro aerial vehicle (MAV) and many more. There are also nonpowered aircraft (gliders) that are capable of navigation and can carry payloads. These are also considered to be UASs. UASs must have an airborne component that can perform a task without a pilot onboard and be capable of controlled and sustained flight [16].

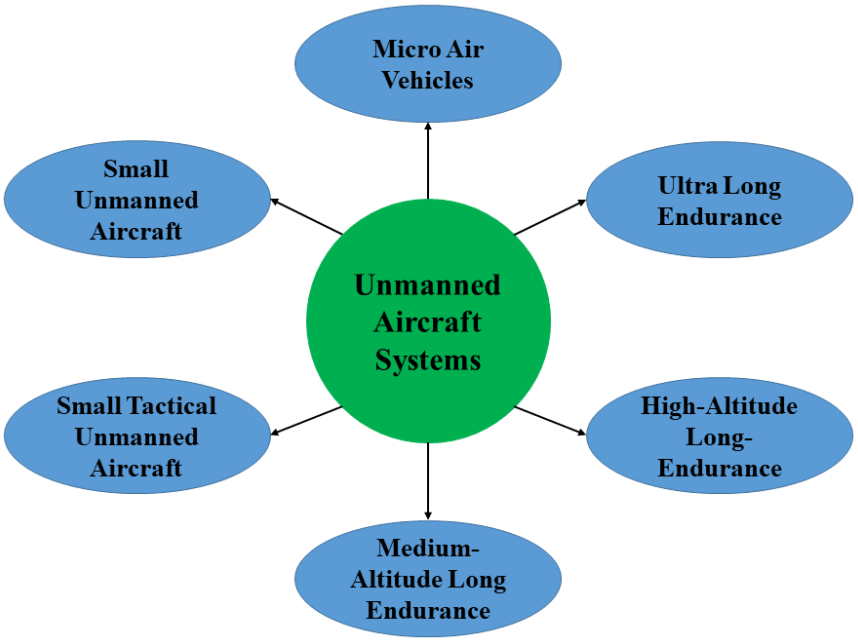

Figure 2: Unmanned aircraft systems categories

As seen in Figure 2, there are many categories of unmanned aircraft systems. Small Unmanned Aircraft Systems (SUAS) are lightweight but still larger than Micro Air Vehicles (MAV). SUAS, MAV, and STUA are generally categorized under Mini UAS and are electrically powered with half an hour to two-hour endurance that are launched by hand or with the help of elastic lines. The

middle and upper weight UAs are medium to long endurance and usually low-altitude; these have taken over the missions of tactical UAs. Ultra-Long Endurance and High-Altitude Long-Endurance UAS were developed later with the advancement of the technologies applied to these UAVs to fly various missions. Now that UAS has been defined and categorized, the history of this technology will be discussed [16].

In the 1980s and early 1990s, operations were revolutionized with advancing technologies in satellite communications, global positioning systems (GPS) and digital electronics. The U.S. military realized at the peak of these technologies, the potential of UASs. In Operation Desert Storm different unmanned systems were used including the Pioneer, hand-launched Pointer, low-cost Exdrone and the high-speed BQM-74E Chukar. With the Pioneer's successful operations in artillery spotting and surveillance, the benefits of using new unmanned aircraft technologies were clear [16].

In the late 1980s DARPA sponsored the Boeing Condor Program, the first UAS to use GPS navigation and auto-landing technology. It set the bar for later systems, capable of enduring 59 hours of operation time and reaching a maximum altitude of 67,000 ft. Following the Condor program, in 1994, three new systems including the General Atomics Predator MALE, Teledyne Ryan Global Hawk (HALE) and the Lockheed DarkStar were developed. These UASs were the first to perform operations that could go beyond line-of-sight using high-bandwidth digital satellite communications links. The United States now became the worlds' leader for UAS technology [16].

Following this development there were few new systems; Predator and Global Hawk systems were the main UASs used in the Air Force. The Army needed successive competitive systems. The Hunter system was selected first but was canceled after it encountered problems during testing. In the following competitive procurement, the Alliant Techsystems Outrider was selected. However, it was also canceled after experiencing development issues. In 2000, AAI Shadow 200 system was the final selection, successfully developed, and used in extensive operations. The Navy also considered numerous systems including an air-launched system, medium-range UAV (MRUAV) which was also canceled after encountering development problems. The FireScout system was then selected around 1990 seeing limited operational service. Around this time the U.S. Naval Research Laboratories (NRL) developed new technologies including miniature digital avionics, GPS-based autopilots, electric propulsion, and micro unmanned aircraft. NASA was also sponsoring an Environmental Research and Sensor Technology (ERAST) program that was tasked with developing high-altitude UASs to gather data of the upper atmosphere. NASA wanted to measure the ozone hole phenomenon, which was an issue that was highly talked about at the time but not well understood. The Aurora Flight Sciences – Perseus, AeroVironment – Pathfinder (solar-powered), General Atomics -Atlus, and Scaled Composites -Raptor were developed under this program. Although these high-altitude UAVs were not used primarily for their original missions, the technologies developed like groundbreaking airframes and propulsion systems had a heavy impact on the advancement of UASs. Another UAS, the Insitu Aerosonde, changed the field in 1999 when it flew across 2000 miles of the Atlantic Ocean on only 1.5 gallons of gas, powered by a four-stroke gasoline engine. The lightweight composite structure and aerodynamic design made history [16].

3.2. Rotorcraft systems

Vertical takeoff and landing air vehicle has a broad range of configurations, which includes rockets, tilted propellers, flapped wing-propeller interactions, shrouded lift fans and etc. Rotorcraft

is one of the underlying VTOL systems that is very well-known and can be operated in a variety of missions such as ISR, antisubmarine warfare, strike, cargo delivery, and sensor emplacement [17]. These configurations are available in many sizes from MAV to manned helicopters. Usually, these configurations are categorized by their number of rotors as follows:

- One rotor or monocopters
- Two rotors
- Three rotors or tricopters
- Four rotors or quadcopters
- Multirotors: hexacopters and octocopter

The latest two categories, quadcopters and multirotor are very common configurations in the realm of small or micro UAVs. One of the main sources of the propulsion in these rotorcraft configurations is the battery-electric source which limits the flight endurance. Another critical disadvantage of VTOL systems is their weight. For a given propulsion class, the thrust dictates a high engines weight.

3.3. Small unmanned aircraft

Small unmanned aircraft is one of the categories of unmanned aircraft systems that suits the application in the bridge construction processes. This system can be both rotorcraft or fixed-wing aircraft and range from 1–55 lb gross weight. SUAS can be larger than MAVs and smaller than small tactical UASs [16].

Sao et al. [18] identified the unmanned aircraft specifications that are necessary for bridge inspections. Their suggestions are as follow:

1. Flying time over 20 min.

2. Additional camera on top of UAS.

3. Camera resolution with low illumination.

4. High video resolution.

5. Payload capacity.

6. UAS lights for extra illumination.

7. Remote range.

8. Ability to fly without global positioning system (GPS) signal.

Most of these characteristics are only beneficial for the inspection process. Drone design parameters vary for different bridge construction and rehabilitation processes. For example, in survey and mapping process the SUAS can fly at a higher altitude and having lights and additional camera on top of the drone will not be helpful. Additionally, the ability to fly without GPS might only be suitable for bridge inspection because the signal can be inaccessible when inspecting under the bridge. However, using GPS for flying at higher altitude results in better and smoother flight.

Following are the SUAS design parameters and tools that can be considered for all of the bridge construction and rehabilitation processes:

- Payload capacity.
- Flight time.
- Transmitter range.
- Speed controller.
- Flight controller.
- Video transmitter.
- Gimbal.

3.4. Current stage of the drone technology: limitations and regulations

The recent researches [19-29] on effectiveness and applications of drones have demonstrated the great potential for drones for inspection of bridges, but at the same time pointed to the technological limitation of existing drone designs preventing their full implementation. Comprehensive and up-to-date knowledge of drone technology is very essential in addressing these limitations. The current commercially available rotorcraft drones are designed for general-purpose application but successful implementation of such systems in bridge inspection requires certain technical considerations.

The current stage of the drone technology has some limitations as well as regulations which limits the utilization of drone in construction and inspection of infrastructure. Figure 3 shows the major limitations that hinder the usage of drones.

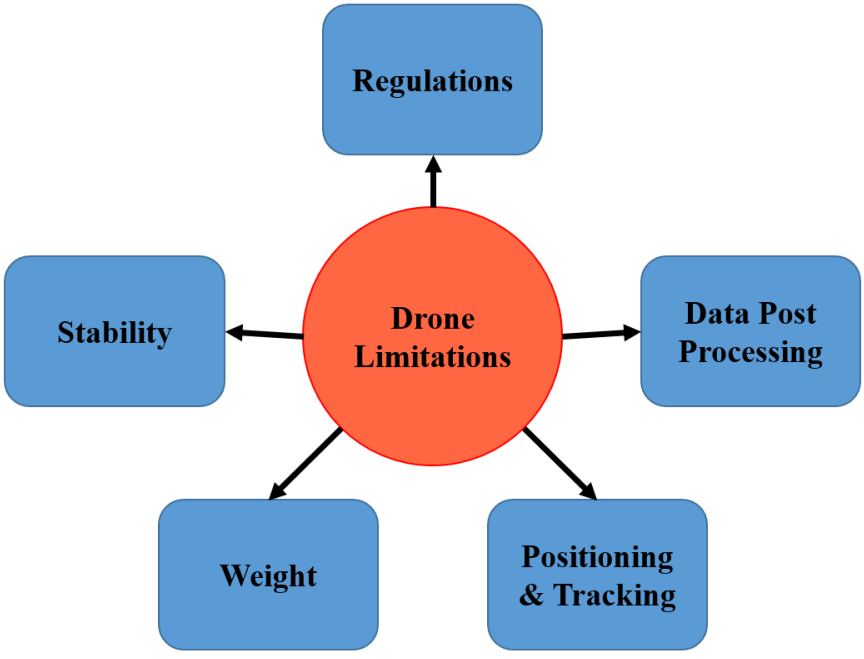

Figure 3: Limitations of current stage of drone usage.

3.4.1. Regulations

To ensure the safety of people present in the drone operation zone and to prevent drones from interfering with the conventional air traffic, the FAA has enforced regulations that limit the

applications of drones [30]. Currently, there are four recognized categories of unmanned aircraft systems (UAS) recognized by FAA: recreational, commercial, governmental and educational [31]. However, considering the growing application of drones in industrial projects, there is a need for specific regulations that take into account the requirements of an industrial site and operations.

3.4.2. Stability

One of the major concerns is the instability of drone due to atmospheric turbulence and gust loads, which can lead to a crash or unreliable data acquisition. The stability of the drone can be enhanced by improving the control system. Metni and Hamel [21] developed a new control law for a quasi-stationary flight based on computer vision for the purpose of bridge maintenance and monitoring of structures, which limits the UAV's orientation to small values of angles and maintain the UAV's stability above a planar object. Additionally, to obtain smooth footage, a Gimbal support could be integrated into the drone, which allows the rotation of the camera about a single axis.

3.4.3. Weight

The use of UAVs with a weight of less than 55 pounds has fewer restrictions and is more convenient [31]. Eschmann et al. [24] studied the use of UAV for the inspection during the building process. They found that while despite the weight limit suggested by FAA, it is possible to put the necessary scanners and cameras on the UAV to obtain accurate pictures and data from the building, without going over the weight limit. They also discussed the necessity to develop and improve anti-collision and navigation systems as well as route planning algorithms to expand the automation of the process.

3.4.4. Positioning and Tracking

While using GPS is one of the major ways to track the flight of drone, Chan et al. [26] suggested the use of Simultaneous Localization and Mapping (SLAM) in order to solve the problem of losing GPS Signal under the bridge. SLAM is a statistical estimation technique where a UAV can build a map of an unknown area, while simultaneously deducing its location within this map. Additional, Yang et al. [27] encountered a problem during inspecting the bridge while using GPS navigation. The problem was the drone became very difficult to fly without a steady GPS signal. To overcome this problem, the researchers implemented laser and image navigation.

3.4.5. Data Post-processing

When the shooting and data acquisition is finished, there should be methods to process the data and obtain the sources of defects and damages. Ellenberg et al. [28] studied different damage conditions such as deformation measurement and crack identification using images provided by UAV. They developed an algorithm that is capable of recognizing other objects in the field of view. Several pictures with cracks that were found online with different complexity were used to verify the algorithm, and then the picture from the UAV. Although there are several complexities in the real-life images from the field of operation such as shadow, noise that this algorithm cannot recognize, it is still a powerful tool to observe the cracks in the structure. Moreover, Seo et al. [29] assessed the damages of an in-service bridge using DJI Phantom 4 drone in the South Dakota state and compared their inspection with the report that was provided by the South Dakota Department of Transportation. They were able to find different types of damages such as cracks, moisture, corrosion and spalling on the concrete, steel, and timber. This study showed the efficiency of using a drone in identifying different types of damages on different materials.

3.5. Pros and cons of rotorcraft and fixed-wing unmanned aircraft systems

Both rotorcraft and fixed-wing aircraft have been used in the construction, survey and mapping, and inspection processes [29]. However, due to their different characteristics, they can be suitable for different processes. One of their major difference is power consumption. "The high thrust dictates a high engine weight within a given propulsion class. The heavy engine reduces the useful load that is composed of payload and fuel weight. Once in forward flight, the thrust requirements diminish, and the large propulsion system often operates at lower efficiency that corresponds to a high fuel flow rate. High fuel consumption and low fuel capacity reduce flight endurance relative to a fixed-wing platform" [16]. Since the major source of lift force for fixed-wing aircraft is their wing, they are more efficient vehicle. Another major difference between fixed-wing drones and rotorcrafts is their flying time. Seo et al. [29] reported several available systems in the market and they compared their characteristics. SenseFly eBee and Topcon Sirius Pro are fixed-wing configurations and can fly for 50 and 55 minutes, respectively, which is almost two times of other presented configurations such as DJI Phantom 4 and DJI Phantom 3 Pro [29]. The major advantageous of rotorcraft are hovering ability and maneuverability. The fact that rotorcrafts can maintain a fixed position in the air make them very suitable for processes such as inspection.

CHAPTER 4. UAV DESIGN: AEROELASTIC TRIM AND STABILITY

4.1. Numerical analysis

Aerospace structures may experience instability during the missions. These instabilities have a different nature. Flutter is a dynamic instability that occurs due to an interaction between aerodynamic, inertial, and elastic forces. In the linear analysis, the p-method, the k-method, and the p-k method are the methods of investigating flutter [32]. On the other hand, in nonlinear aeroelasticity, flutter is usually interpreted as a limit cycle oscillation (LCO), and methods from the study of dynamical systems can be used to determine the speed at which flutter will occur.

In June 2003 the Helios prototype, which was a highly flexible ultra-lightweight flying wing, crashed during the flight test. During the flight, the aircraft experienced normal turbulence, which led to an unexpected high wing dihedral. Then the aircraft became unstable and the leading edge failed. One of the reasons behind the crash was reported as: "Lack of adequate analysis methods led to an inaccurate risk assessment of the effects of configuration changes leading to an inappropriate decision to fly an aircraft configuration highly sensitive to disturbances"[33].

Flutter is a very complex problem that may change with minor changes in the structure. Even adding a small object such as a camera or a sensor can change the boundary of the instability of a flying wing.

HALE aircraft usually has high-aspect-ratio and very flexible wings. These wings may undergo large deflections which result in geometrically nonlinear behavior and also they are prone to aeroelastic instabilities such as flutter, divergence and limit cycle oscillations. The computer program NATASHA (Nonlinear Aeroelastic Trim And Stability of High Altitude Long Endurance Aircraft) is a powerful tool for the simulation of aeroelastic behavior of very flexible high-aspect-ratio wings. It is based on the nonlinear composite beam theory of Hodges [34] that accommodates the modeling of high-aspect-ratio wings. The developers of NATASHA used the aerodynamic theory of Peters et al. [35] to model the aerodynamic forces and the p method to evaluate the aeroelastic stability. The basic theory, assumptions and formulation of for this approach is described in the following. It should be pointed out that the referenced software and approach targets fixed-wing aircrafts. Modifications and new developments are required for application of a similar software to rotorcrafts.

4.1.1. Nonlinear Composite beam theory

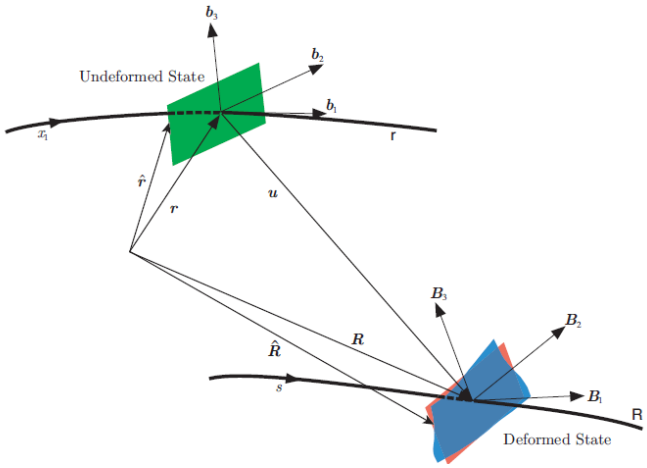

Figure 4: Sketch of beam kinematics [36-38].

The fully intrinsic nonlinear composite beam theory [34] is based on first-order partial differential equations of motion that are independent of displacement and rotation variables. They contain variables that are expressed in terms of the bases of the reference frames for the undeformed and deformed beams, $b(x_1)$ and $B(x_1, t)$, respectively, as seen in Figure 4. These equations are based on force, moment, angular velocity, and linear velocity with nonlinearities of second order. The equations of motion are [36-38]:

$$\begin{aligned} F_B' + \tilde{K}_B F_B + f_B &= \dot{P}_B + \tilde{\Omega}_B P_B, \\ M_B' + \tilde{K}_B M_B + \left(\tilde{e}_1 + \tilde{\gamma}\right) F_B + m_B &= \dot{H}_B + \tilde{\Omega}_B H_B + \tilde{V}_B P_B, \end{aligned} \tag{1}$$

In this set of equations, F_B and M_B are column matrices of cross-sectional stress and moment resultant measures in the B frame, respectively; V_B and Ω_B are column matrices of cross-sectional frame velocity and angular velocity measures in the B frame, respectively; P_B and H_B are column matrices of cross-sectional linear and angular momentum measures in the B frame, respectively; and K is the column matrix of deformed beam's curvature and twist measures in $\mathbf{B}_i$ basis. The generalized strains and velocities are related to stress resultants and moments by the structural constitutive equations as follow [36-38]:

$$\begin{Bmatrix} \gamma \\ \kappa \end{Bmatrix} = \begin{bmatrix} R & S \\ S^T & T \end{bmatrix} \begin{Bmatrix} F_B \\ M_B \end{Bmatrix} \tag{2}$$

Here, R_{11} ... T_{33} are cross-sectional flexibility coefficients. The inertial constitutive equations can be presented as [36-38]:

$$\begin{Bmatrix} P_B \\ H_B \end{Bmatrix} = \begin{bmatrix} \mu\Delta & -\mu\tilde{\xi} \\ \mu\tilde{\xi} & I \end{bmatrix} \begin{Bmatrix} V_B \\ \Omega_B \end{Bmatrix} \tag{3}$$

where ξ is the offset from the reference line of the cross-sectional mass centroid; μ is the mass per unit length, and I is the cross-sectional mass moments of inertia [36-38].

The intrinsic kinematical partial differential equations are derived [34], which are given as:

$$\begin{aligned} V_B' + \tilde{K}_B V_B + \left(\tilde{e}_1 + \tilde{\gamma}\right)\Omega_B &= \dot{\gamma}, \\ \Omega_B' + \tilde{K}_B \Omega_B &= \dot{\kappa}, \end{aligned} \tag{4}$$

4.1.2. Finite state-induced model of Peters et al.

The aerodynamic model of Peters et al. [35] is utilized in this study. This finite state model is a state-space, thin-airfoil, inviscid, incompressible approximation of an infinite-state representation of the aerodynamic loads. By using known airfoil parameters, it can consider induced flow in the wake and apparent mass effects. Additionally, it can accommodate large motion of the airfoil as well as the deflection of a small trailing-edge flap. Although this model cannot simulate the three-dimensional effects associated with the wing tip, it can accurately approximate the aerodynamic loads acting on high-aspect-ratio wings. The lift, drag and pitching moment at the quarter-chord are given by [36-38]

$$\begin{aligned} L_{aero} &= \rho b\left[\left(c_{l_0} + c_{l_\beta}\beta\right)V_T V_{a_2} - c_{l_\alpha}\dot{V}_{a_3} b/2 - c_{l_\alpha} V_{a_2}\left(V_{a_3} + \lambda_0 - \Omega_{a_1} b/2\right) - c_{d_0} V_T V_{a_3}\right], \\ D_{aero} &= \rho b\left[-\left(c_{l_0} + c_{l_\beta}\beta\right)V_T V_{a_3} + c_{l_\alpha}\left(V_{a_3} + \lambda_0\right)^2 - c_{d_0} V_T V_{a_2}\right], \\ M_{aero} &= 2\rho b\left[\left(c_{m_0} + c_{m_\beta}\beta\right)V_T - c_{m_\alpha} V_T V_{a_3} - bc_{l_\alpha}/8 V_{a_2}\Omega_{a_1} - b^2 c_{l_\alpha}\dot{\Omega}_{a_1}/32 + bc_{l_\alpha}\dot{V}_{a_3}/8\right], \end{aligned} \tag{6}$$

Here,

$$\begin{aligned} V_T &= \sqrt{V_{a_2} + V_{a_3}}, \\ \sin\alpha &= \frac{-V_{a_3}}{V_T}, \\ \alpha_{rot} &= \frac{\Omega_{a_1} b/2}{V_T}, \end{aligned} \tag{7}$$

and β is the angle of flap deflection, V_{a2} and V_{a3} denote the measure numbers of V_a. The effect of unsteady wake (induced flow) and apparent mass included as λ_0 and acceleration terms in the force and moment equation [36-38], which λ_0 can be calculated using the induced flow model of Peters et al. [35].

$$\lambda_0 = \frac{1}{2}\{b\}^T \{\lambda\},$$
$$[A]\{\dot{\lambda}\} + \left(\frac{V_T}{b}\right)\{\lambda\} = \left(-\dot{V}_{a_3} + \frac{b}{2}\dot{\Omega}_{a_1}\right)\{c\}, \quad (8)$$

Here λ defines the column matrix of induced flow states, and [A], [b], and [c] represents constant matrices [36-38], which are derived in Ref. [35].

4.1.3. Aeroelastic stability results and discussion

Mardanpour et al. [36] studied the effects of engine placement on nonlinear aeroelastic gust response of a very flexible high aspect-ratio wing using the computer program NATASHA (Nonlinear Aeroelastic Trim And Stability of HALE Aircraft). They reported that the engine placement can increase the flutter speed significantly and enhances the stability of the aircraft (see Figure 5).

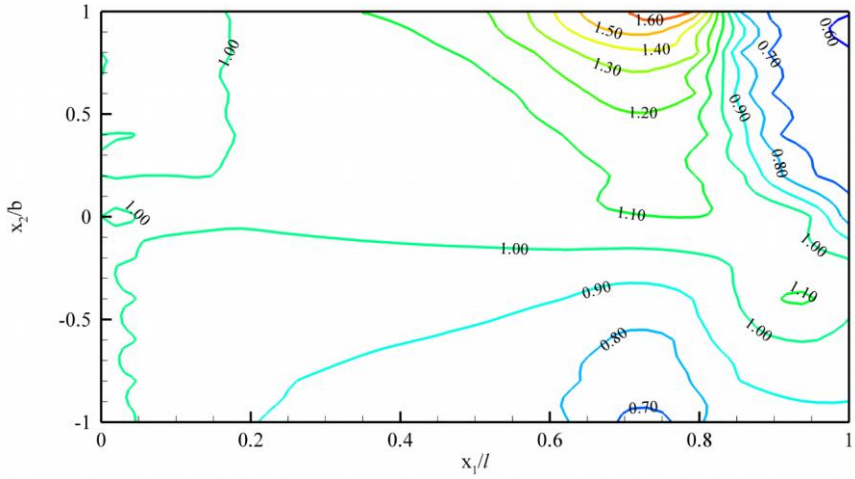

Figure 5: Contour of normalized flutter speed for engine placement in chord wise direction [36].

Additionally, gust load is a load that causes large excitations and the analysis of gust responses are required in the design of aircraft. In the case of a highly flexible aircraft, these excitations are even more important. Mardanpour et al. [36, 37] reported that for the engine placement along the span with offsets from the elastic axis, engine placement significantly affects gust response of the wing and can be used as a gust load alleviation method. The results of their study are available in Figure 6.

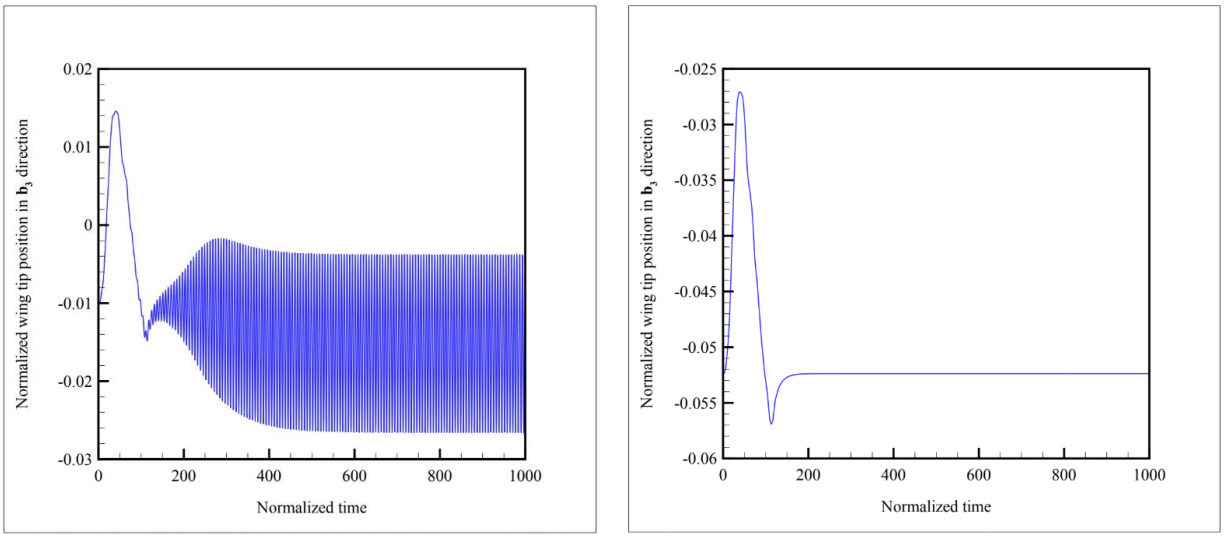

(a) (b)

Figure 6: Normalized magnitude of the wing tip position in the b_3 direction vs. normalized time. (a) Engine placement at the root, (b) Engine placement at 75% of the span forward of reference line [37].

Moreover, Izadpanahi and Mardanpour [38] studied the effects of gust loads on the nonlinear aeroelastic stability of a flying wing aircraft with very flexible wings. They found the same physical phenomenon happens in a full aircraft configuration and a correct choice of engine location can suppress the aeroelastic instabilities due to gust loads (see Figure 7).

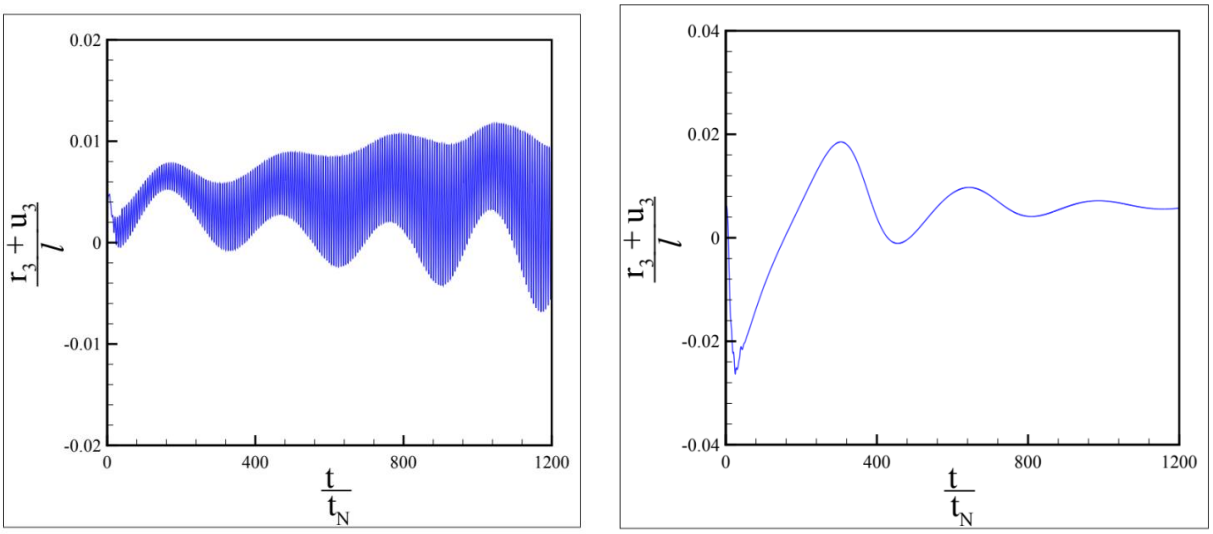

(a) (b)

Figure 7: Normalized magnitude of the wing tip position in the b_3 direction vs. normalized time. (a) Engine placement at the root, (b) Engine placement at 60% of the span forward of reference line [38].

4.1.4. Customization of NATASHA for UAV for Survey and Inspection

NATASHA can be customized for different configurations through several variables. The list of variables can be found in the Appendix A section of this report. In this section, we will present some explanations on how to customized NATASHA for a flying wing. The schematic view of the flying wing is available in Figure 8.

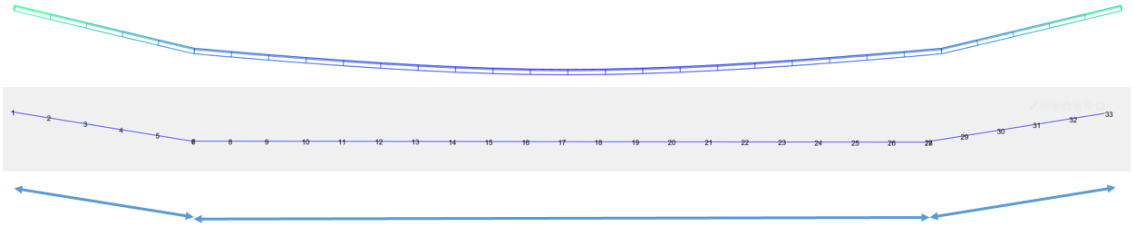

Figure 8: Flying wing example in NATASHA

- **Geometry and property settings**

This figure shows a flying wing configuration with three beams. Using *Nb*, the number of beams in NATASHA can be specified. Then for each beam, the number of elements should be identified as *N*= [first beam elements; second beam elements; third beam elements], which for this example is *N*= [5;20;5]. It is worth mentioning that because the beam theory is geometrically exact, there is no need for an excessive number of elements. Using a few elements accurate results can be obtained. The variable that can be used to assign the length of each element is *dl*, which will be in the form of a vector.

The flexibility matrix is shown in the structural constitutive equation, Eq. (2), can be defined in the program using *R*, *S*, and *T* matrices in the input file as well as the mass matrix in the inertial constitutive equation, Eq. (3), with *mu*, *xi*, *II* variables.

- **Solution settings**

The next variable to modify is the *btype* which will be a vector with a number of rows equal to the number of beams. Each row should either be 1 representing lifting surface or 2 indicating a slender body. This example the *btype* will be written as *btype* = [1;1;1] because all three beams are lifting surfaces.

BC_flag0 is the parameter that identifies the boundary condition. For the current example which is a full aircraft free-free case, *BC_flag0* should be equal to 0. The case of full aircraft configuration can be trimmed in two different ways with *Trim_flag* parameter. The case of *Trim_flag* = 0 uses the control values such as thrust and flap deflection to calculate the speed of the flight, while *Trim_flag* = 1 uses the ratio of aircraft speed over the angle of flight to calculate the required flight control values, i.e. engine thrust and flap deflection.

- **Aerodynamic settings**

The aerodynamic theory behind NATASHA uses known airfoil parameters. In order to give the aerodynamic properties to code first, we need to define the chord and the aerodynamic center. For lifting surfaces, *b* identifies the semi-chord. *y_ac* for the lifting surface is the distance between the aerodynamic center and the reference line of the beam. The parameter that assigns the value of the aerodynamic coefficients is *C_aero*. It has the aerodynamic coefficients of the airfoil.

- **Pod settings**

The addition of any sensors can be considered by using the Pod settings. The Pod variables such as mass, location, offset and aerodynamic properties can be assigned using the following variables.

muhat is a vector for identifying any nodal mass such as the engine, camera or any other payloads. *IIhat* is a 3 by *NN* matrix and represents the moment of inertia. The offset from the reference line can be considered by *xihat*. Additionally, the aerodynamic characteristics can be inputted by *bpod*, *lpod*, *ypod_ac*, *Cpod_a*, and *Cpod_aero*. The detailed explanation of these variables is available in Appendix A.

4.1.5. Customized version of NATASHA for DOT engineers

In this section, a customized version of the generic fixed-wing aircraft is presented so that the DOT engineers are capable to use to assess the stability of the aircraft. This example shows how the sensors and cameras can be integrated into NATASHA. In this example, there are three pods at nodes 7,17 and 27. The masses of these pods are assigned with *muhat*. If these pods are mounted with an offset from the reference line, the offset can be defined by *xihat*. Here, the offset for the pods at nodes 7 and 27 are defined by podz which is only in $\boldsymbol{b_3}$ direction, and the other directions are 0. Also, for node 17 the offset in $\boldsymbol{b_2}$ and $\boldsymbol{b_3}$ directions are assigned by *centery* and *centerz*. Using *podz*, *centery* and *centerz*, the mass moment of inertia of the pods *IIhat* can be evaluated.

- Example 1: Flying wing

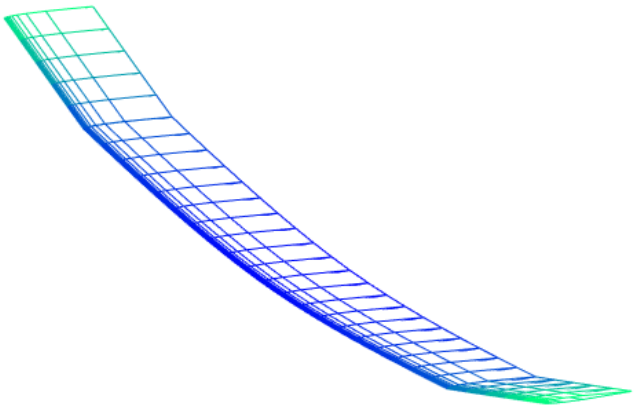

Figure 9: Flying wing configuration

Input file variables:

```
rho = 2.3769*10^(-3);
gg = 32.2;
unsteady_aero_flag = 1;
no_eig_val =10;
sweep_flag=0;
no_cont = 2;
cont_values = [8.4069;0.0952];
cont_values = [10;7];
Trim_flag = 1;
    UU =40 ;
    phi =0 ;
Analysis_flag = 1;
gust_var_flag = 2;
gust_var_flag = 2;
gust_quantity = [3 2;4 2;1 3; 2 3;3 1;4 1;5 3];
gust_freq = logspace(-3,1,100)';
prior_soln_flag = 1;
    U_inf = UU;
    alpha_inf = 6*pi/180;
    pitch_inf = 6*pi/180;
NR_auto_damp = 1;
NR_max_half = 10;
NR_maxiter = 100;
NR_feps = 10.0^(-10);
NR_xeps = 10.0^(-8);
Nb = 3;
ref_beam0 = 2;
ref_node0 = 11;
BC_flag0 = 0;
    Clr_ref = eye(3);
btype = [1;1;1];
N = [5;20;5];
NN = sum(N)+Nb;
dl = 8;
dl = repmat(dl,1,NN);
k = zeros(3,NN);
flexibility_flag = 1;
R = [0.0 0.0 0.0;0.0 0.0 0.0;0.0 0.0 0.0]*flexibility_flag;
R = repmat(R,[1 1 NN]);
S = [0.0 0.0 0.0;0.0 0.0 0.0;0.0 0.0 0.0]*flexibility_flag;
S = repmat(S,[1 1 NN]);
T = [1/(0.4*10.0^6) 0.0 0.0;0.0 1.0/(2.5*10.0^6) 0.0;0.0 0.0
1.0/(30*10.0^6)]*flexibility_flag;
T = repmat(T,[1 1 NN]);
clear flexibility_flag
mu = 6/32.2;
mu = repmat(mu,[1 NN]);
xi = [0.0; 0.0; 0.0];
xi = repmat(xi,[1 NN]);
II = [30 0.0 0.0;0.0 5 0.0;0.0 0.0 25]/32.2;
II = repmat(II,[1 1 NN]);
Clrhat = repmat(eye(3),[1 1 NN]);
```

```
podmass = 50;
payloadmass = 190;
centermass = (60+payloadmass);
podz = -3;
centerz = -3;
centery = 0;
muhat = zeros(1,NN);
xihat = zeros(3,NN);
IIhat = zeros(3,3,NN);
muhat(7) = podmass/32.2;
muhat(27) = podmass/32.2;
muhat(17) = centermass/32.2;
xihat(:,7) = [0;0;podz];
xihat(:,27) = [0;0;podz];
xihat(:,17) = [0;centery;centerz];
IIhat(:,:,7) = podmass/32.2*podz^2*[1 0.0 0.0;0.0 1 0.0;0.0 0.0 0.0];
IIhat(:,:,27) = podmass/32.2*podz^2*[1 0.0 0.0;0.0 1 0.0;0.0 0.0 0.0];
IIhat(:,:,17) = centermass/32.2*[centerz^2+centery^2 0.0 0.0;0.0 centerz^2 -
centerz*centery;0.0 -centerz*centery centery^2];
clear podmass
clear centermass
clear podz
clear centerz
fhat_T = zeros(3,NN);
mhat_T = zeros(3,NN);
Hhat_eng = zeros(3,NN);
cont_no_T = repmat(no_cont+1,[1 NN]);
fhat_T(:,7) = [0.0; 1.0; 0.0];
fhat_T(:,12) = [0.0; 1.0; 0.0];
fhat_T(:,17) = [0.0; 1.0; 0.0];
fhat_T(:,22) = [0.0; 1.0; 0.0];
fhat_T(:,27) = [0.0; 1.0; 0.0];
cont_no_T(7) = 1;
cont_no_T(12) = 1;
cont_no_T(17) = 1;
cont_no_T(22) = 1;
cont_no_T(27) = 1;
b = 4;
b = repmat(b,[1 NN]);
y_ac = 0.0;
y_ac = repmat(y_ac,[1 NN]);
y_ac_graph = y_ac;
C_a = repmat(eye(3),[1 1 NN]);
C_aero = [0.0; 2*pi; 1; 0.01; 0.0; 0.0; 0.025; 0.0; -0.25; 0.0];
C_aero = repmat(C_aero,[1 NN]);
cont_no_beta = 2;
cont_no_beta = repmat(cont_no_beta,[1 NN]);
cont_no_sym = ones(1,NN);
bpod = repmat(0,[1 NN]);
bpod(7) = 4;
bpod(27) = 4;
bpod(17) = 4;
lpod = repmat(0,[1 NN]);
lpod(7) = 6;
lpod(27) = 6;
lpod(17) = 6;
ypod_ac = repmat(0,[1 NN]);
```

```
Cpod_a = repmat(eye(3),[1 1 NN]);
Cpod_aero = [5; 0.02];
Cpod_aero = repmat(Cpod_aero,[1 NN]);
beam_conn = [2 0; 1 1; 3 2];
NBC = 2;
BC_beam1 = [2; 2];
BC_node1 = [1; 21];
BC_beam2 = [1; 3];
BC_node2 = [6; 1];
dihedral = 10*pi/180;
BC_C(1:3,1:3,1) = [cos(dihedral) 0 -sin(dihedral);0 1 0;sin(dihedral) 0
cos(dihedral)];
BC_C(1:3,1:3,2) = [cos(dihedral) 0 -sin(dihedral);0 1 0;sin(dihedral) 0
cos(dihedral)]';
```

- Example 2: Swept flying wing

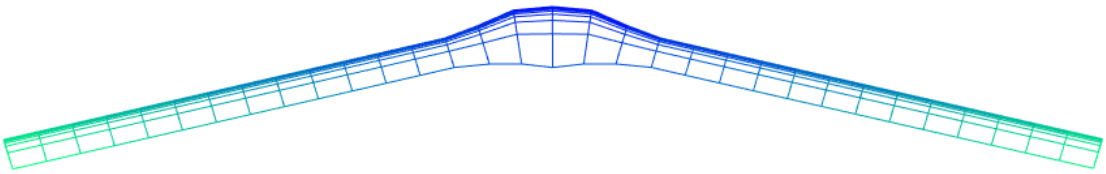

Figure 10: Swept Flying wing configuration

Input file:

```
rho =0.4135;
gg = 9.8;
no_cont = 2;
cont_values = [1000; 6*pi/180];
no_eig_val= 50;
Analysis_flag = 0;
unsteady_aero_flag = 1;
Trim_flag = 1;
    UU = 30;
    phi = 0*pi/180;
    prior_soln_flag = 1;
    U_inf = UU;
    alpha_inf = 6*pi/180;
    pitch_inf = 6*pi/180;
NR_auto_damp = 1;
NR_max_half = 10;
NR_maxiter = 100;
NR_feps = 10.0^(-4);
NR_xeps = 10.0^(-4);
Nb = 1;
btype = [1];
BC_flag0 = 0;
```

```
Clr_ref = eye(3);
N = [2*16];
NN = sum(N)+Nb;
ref_beam0 = 1;
ref_node0 =(N/2)+1;
k = zeros(3,NN);
Clrhat = repmat(eye(3),[1 1 NN]);
Cbihat_r = repmat(eye(3),[1 1 NN]);
rrhat = zeros(3,NN);
mu = repmat(0,[1 NN]);
xi = [0.0; 0.0; 0.0];
xi = repmat(xi,[1 NN]);
II = [0 0.0 0.0;0.0 0 0.0;0.0 0.0 0];
II = repmat(II,[1 1 NN]);
R = [0.0 0.0 0.0;0.0 0.0 0.0;0.0 0.0 0.0];
R = repmat(R,[1 1 NN]);
S = [0.0 0.0 0.0;0.0 0.0 0.0;0.0 0.0 0.0];
S = repmat(S,[1 1 NN]);
T = [0 0.0 0.0;0.0 0 0.0;0.0 0.0 0];
T = repmat(T,[1 1 NN]);
dl(1:NN) = 0;
b(1:NN) = 0;
dl(:) = 1.0;
 b(:)= 0.5;
ij=N/2+1;
for i = 1:N/2
    ij= ij-1;
    k(:,i) = [0;0;0];
    Clrhat(:,:,i) = eye(3);
    R(:,:,i) = [7.2432117344e-09 0  0; 0 2.5801976218e-08 1.7568794365e-13;0
1.7568794365e-13  9.6612428291e-07];
    S(:,:,i) = [0  -7.5468385916e-15  7.3704693316e-09; -3.3393365227e-14  0
0;-1.1608670353e-06  0  0];
    T(:,:,i) = [3.4795687168e-06  0 0;0 4.265980174e-06 -6.6640482794e-14; 0
-6.6640482794e-14  6.5087963473e-08];
    mu(1,i) = 1.5604056027;
    xi(:,i) = [0 ; 0.113238591872687  ; 1.25305050764799e-17];
    II(:,:,i) = [0.17597195528  0  0; 0  0.0023358158057  -3.9000176218e-18;
0 -3.9000176218e-18 0.17363613948];
end
ij=N/2+1;
for i = N/2+1:N
    ij= ij-1;
    k(:,i) = k(:,ij);
    Clrhat(:,:,i) = Clrhat(:,:,ij);
    R(:,:,i) = R(:,:,ij);
    S(:,:,i) = S(:,:,ij);
    T(:,:,i) = T(:,:,ij);
    mu(1,i) = mu(1,ij);
    xi(:,i) = xi(:,ij);
    II(:,:,i) = II(:,:,ij);
end

for ii=N/2-1:N/2+2
    dl(ii) = 1.0;
    R(:,:,ii) = R(:,:,1);
    S(:,:,ii) = S(:,:,1);
```

```
    T(:,:,ii) = T(:,:,1);
    mu(1,ii) = 4.0*mu(1,1);
    xi(:,ii) = xi(:,1);
    II(:,:,ii) =II(:,:,1);
end
b(N/2-1)= 0.8;
b(N/2)= 1.0;
b(N/2+1)= 1.0;
b(N/2+2)= 0.8;
flexibility_flag =0;
if flexibility_flag ==1
R = R*0;
S = S*0;
T = T*0;
end
Sweepangle=15;
Clrhat = repmat(eye(3),[1 1 NN]);
Cbihat_r = repmat(eye(3),[1 1 NN]);
rrhat = zeros(3,NN);
sweep_flag=1;
if  sweep_flag==1;
    sweep_node=N/2+2;
    SA = (-Sweepangle)*pi/180;
    Clrhat(:,:,sweep_node)=[cos(SA) -sin(SA) 0; sin(SA) cos(SA) 0; 0 0 1];
end
for nn = ref_node0+1 : NN
    Cbihat_r(:,:,nn) = Clrhat(:,:,nn)'*inv(eye(3)/dl(nn-1) + ...
        tilde(k(:,nn-1))/2)*(eye(3)/dl(nn-1) - ...
        tilde(k(:,nn-1))/2)*Cbihat_r(:,:,nn-1);
    rrhat(:,nn) = rrhat(:,nn-1) + (Cbihat_r(:,:,nn-1) + ...
        Clrhat(:,:,nn)*Cbihat_r(:,:,nn))'*[1;0;0]*dl(nn-1)/2;
end
if  sweep_flag==1;
    sweep_node=N/2 ;
    SA = (-Sweepangle)*pi/180;
    Clrhat(:,:,sweep_node)=[cos(SA) -sin(SA) 0; sin(SA) cos(SA) 0; 0 0 1];
end

for nn = ref_node0-1:-1:1
    Cbihat_r(:,:,nn) = inv(eye(3)/dl(nn) -...
        tilde(k(:,nn))/2)*(eye(3)/dl(nn) +...
        tilde(k(:,nn))/2)*Clrhat(:,:,nn+1)*Cbihat_r(:,:,nn+1);
    rrhat(:,nn) = rrhat(:,nn+1) - (Cbihat_r(:,:,nn) +...
        Clrhat(:,:,nn+1)*Cbihat_r(:,:,nn+1))'*[1;0;0]*dl(nn)/2;
end
y_ac(1:NN)=0.5*b(1:NN);
y_ac_graph = y_ac;
C_a = repmat(eye(3),[1 1 NN]);
C_aero = [0.0; 2*pi; 1.0; 0.01; 0.0; 0.0; 0.0; -0.08; 0.0; 0.0];
C_aero = repmat(C_aero,[1 NN]);
cont_no_beta = 3;
cont_no_beta = repmat(cont_no_beta,[1 NN]);
cont_no_sym(1:NN)= ones(1,NN);
cont_no_beta(1:NN)=2;
bpod = repmat(0,[1 NN]);
lpod = repmat(0,[1 NN]);
ypod_ac = repmat(0,[1 NN]);
```

```
Cpod_a = repmat(eye(3),[1 1 NN]);
Cpod_aero = [0; 0];
Cpod_aero = repmat(Cpod_aero,[1 NN]);
fhat_T = zeros(3,NN);
mhat_T = zeros(3,NN);
Hhat_eng = zeros(3,NN);
cont_no_T = repmat(no_cont+1,[1 NN]);
muhat = zeros(1,NN);
xihat = zeros(3,NN);
IIhat = zeros(3,3,NN);
Eng1_NN=16;
Eng2_NN=18;
muhat_engine= 5;
cont_no_T(Eng1_NN)    = 1;
cont_no_T(Eng2_NN)    = 1;
muhat(Eng1_NN)=  muhat_engine;  % [Kg/m]
muhat(Eng2_NN)=  muhat_engine;  % [Kg/m]
fhat_T(:,Eng1_NN)= Cbihat_r(:,:,Eng1_NN) * [0.0; 1.0; 0.0];
fhat_T(:,Eng2_NN)= Cbihat_r(:,:,Eng2_NN) * [0.0; 1.0; 0.0];
beam_conn = [1 1];
NBC =0;
```

- Example 3: UAV with fuselage

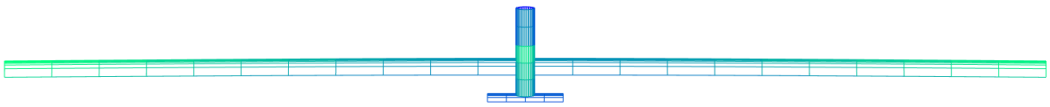

Figure 11: UAV with fuselage configuration

Input file:

```
rho = 0.0889;
gg = 9.81;
unsteady_aero_flag = 1;
no_cont = 3;
cont_values = [5;-0.5;0.0];
sweep_flag=0;
Trim_flag = 1;
    UU = 20;
    phi = 0;
Analysis_flag = 0;
gust_var_flag = 2;
gust_quantity = [3 2;4 2;1 3; 2 3;3 1;4 1;5 3];
gust_freq = logspace(-2,2,100)';
prior_soln_flag = 1;
soln_file = 'soln.mat';
    U_inf = UU;
    alpha_inf = 6*pi/180;
    pitch_inf = 6*pi/180;
NR_auto_damp = 1;
NR_max_half = 10;
NR_maxiter = 100;
```

```
NR_feps = 10.0^(-8);
NR_xeps = 10.0^(-6);
Nb = 3;
ref_beam0 = 1;
ref_node0 = 12;
BC_flag0 = 0;
Clr_ref = eye(3);
btype = [1;2;1];
N = [22;5;4];
NN = sum(N)+Nb;
dl(1:23) = repmat(2.5,1,23);
dl(24:29) = repmat(1,1,6);
dl(30:34) = repmat(1,1,5);
k = zeros(3,NN);
R = [0.0 0.0 0.0;0.0 0.0 0.0;0.0 0.0 0.0];
R = repmat(R,[1 1 NN]);
S = [0.0 0.0 0.0;0.0 0.0 0.0;0.0 0.0 0.0];
S = repmat(S,[1 1 NN]);
T = [1/(1.0*10.0^4) 0.0 0.0;0.0 1.0/(5*10.0^5) 0.0;0.0 0.0 1.0/(4.0*10.0^6)];
T(1:3,1:3,1:23) = repmat(T,[1 1 23]);
T(1:3,1:3,24) = [1/(1.0*10.0^6) 0.0 0.0;0.0 1.0/(2.0*10.0^6) 0.0;0.0 0.0
1.0/(4.0*10.0^8)];
T(1:3,1:3,24:29) = repmat(T(:,:,24),[1 1 6]);
T(1:3,1:3,30) = [1/(1.0*10.0^4) 0.0 0.0;0.0 1.0/(2.0*10.0^5) 0.0;0.0 0.0
1.0/(4.0*10.0^6)];
T(1:3,1:3,30:34) = repmat(T(:,:,30),[1 1 5]);
mu(1:23) = repmat(0.75,[1 23]);
mu(24:29) = repmat(4,[1 6]);
mu(30:34) = repmat(0.1,[1 5]);
xi = [0.0; 0.0; 0.0];
xi = repmat(xi,[1 NN]);
II = 0.75/12*[(1)^2+(0.1)^2 0.0 0.0;0.0 (0.1)^2+(1)^2 0.0;0.0 0.0
(1)^2+(1)^2];
II(1:3,1:3,1:23) = repmat(II,[1 1 23]);
II(1:3,1:3,24) = 4*[6*(0.5)^2 0.0 0.0;0.0 3*(0.5)^2+(1)^2 0.0;0.0 0.0
3*(0.5)^2+(1)^2];
II(1:3,1:3,24:29) = repmat(II(:,:,24),[1 1 6]);
II(1:3,1:3,30) = 0.1/12*[(1/2)^2+0.1^2 0.0 0.0;0.0 0.1^2+(1)^2 0.0;0.0 0.0
(1/2)^2+(1)^2];
II(1:3,1:3,30:34) = repmat(II(:,:,30),[1 1 5]);
Clrhat = repmat(eye(3),[1 1 NN]);
muhat = zeros(1,NN);
xihat = zeros(3,NN);
IIhat = zeros(3,3,NN);
fhat_T = zeros(3,NN);
mhat_T = zeros(3,NN);
Hhat_eng = zeros(3,NN);
cont_no_T = repmat(no_cont+1,[1 NN]);
fhat_T(:,10) = [0.0; 1.0; 0.0];
fhat_T(:,14) = [0.0; 1.0; 0.0];
cont_no_T(10) = 1;
cont_no_T(14) = 1;
b(1:23) = repmat(0.5,[1 23]);
b(24:29) = repmat(0.5,[1 6]);
b(30:34) = repmat(0.25,[1 5]);
y_ac(1:23) = repmat(-0.05,[1 23]);
y_ac(24:29) = repmat(0.0,[1 6]);
```

```
y_ac(30:34) = repmat(-0.025,[1 5]);
C_a = repmat(eye(3),[1 1 NN]);
C_aero = [0.0;  6.37;     0.979;    0.0092; 0.0;          0.0; -0.026; 0.0;
-0.226;   0.0];
C_aero(:,1:23) = repmat(C_aero,[1 23]);
C_aero(:,24) = [0.0;  2*pi;     0.015;    1.2; 0.0;          0.0; 0.0; 0.0;
0.0;   0.0];
C_aero(:,24:29) = repmat(C_aero(:,24),[1 6]);
C_aero(:,30) = [0.0; 6.37; 0.979; 0.0092; 0.0; 0.0;  0.0; 0.0; -0.226; 0.0];
C_aero(:,30:34) = repmat(C_aero(:,30),[1 5]);
cont_no_beta(1:23) = repmat(2,[1 23]);
cont_no_beta(24:29) = repmat(no_cont+1,[1 6]);
cont_no_beta(30:34) = repmat(3,[1 5]);
cont_no_sym = ones(1,NN);
bpod = repmat(0,[1 NN]);
bpod(32) = 2;
lpod = repmat(0,[1 NN]);
lpod(32) = 4;
ypod_ac = repmat(0,[1 NN]);
ypod_ac(32) = -0.05;
Cpod_a = repmat(eye(3),[1 1 NN]);
Cpod_aero = [5.54; 0.0082];
Cpod_aero = repmat(Cpod_aero,[1 NN]);
beam_conn = [1 0; 2 1; 3 2];
NBC = 2;
BC_beam1 = [1; 2];
BC_node1 = [12; 6];
BC_beam2 = [2; 3];
BC_node2 = [4; 3];
BC_C(1:3,1:3,1) = [0 -1 0;
    1 0 0;
    0 0 1];
BC_C(1:3,1:3,2) = [0 1 0;
    -1 0 0;
    0 0 1];
```

4.2. Example of rotorcraft implementation for survey and inspection

In order to investigate the performance of the drone in operation while carrying the hardware required for bridge construction and rehabilitation projects, we modeled the weight and geometry of a typical sensor with a payload. The payload was mounted on the drone, which created an asymmetric loading state (see Figure 12).

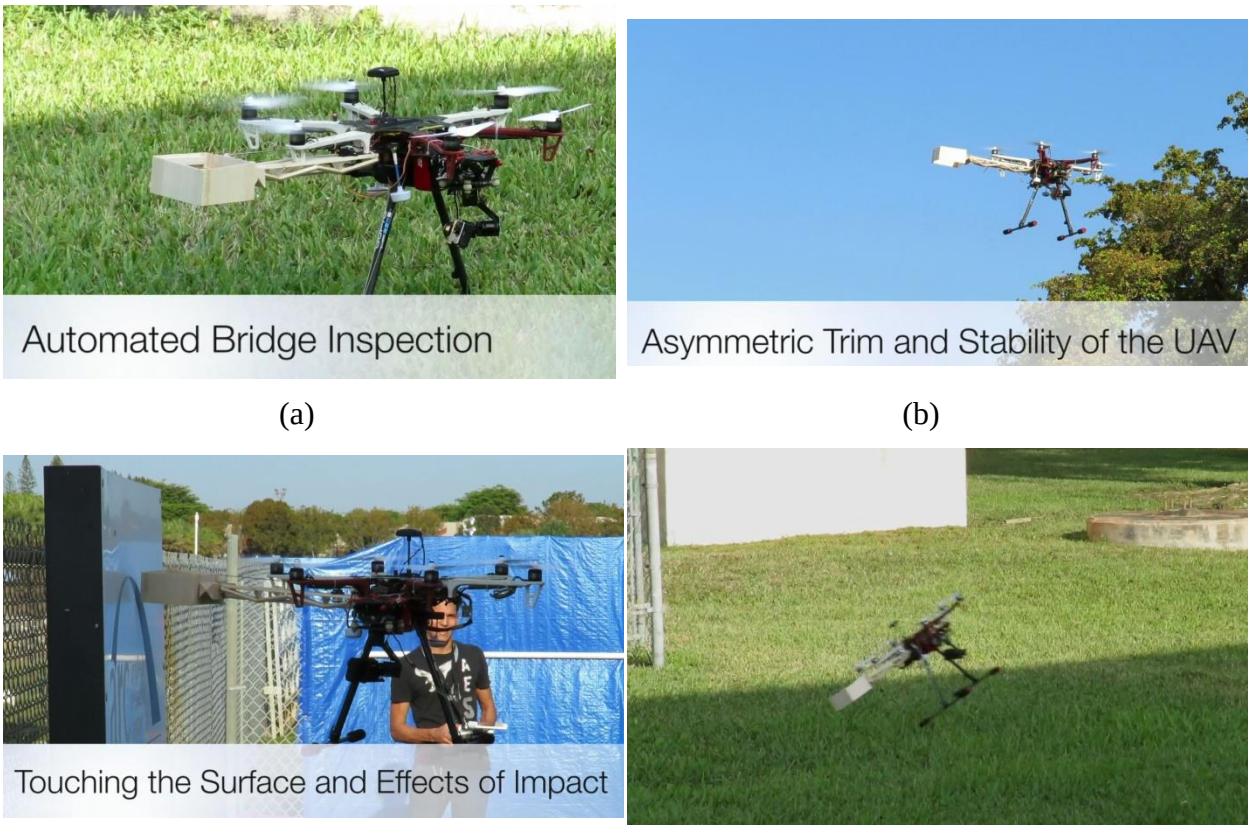

(a) (b)

(c) (d)

Figure 12: A bridge inspection drone prototype (a) the sensor model mounted on the drone and ready for take-off (b) drone performing stable flight with asymmetric payload (d) investigating the effect of impact on flight stability (d) investigating the effect of gust loads on inspecting drones with asymmetric loading.

The carried out inspection missions show that special attention should be given to suppressing gust and impact load. Also, the use of stabilizing mounts for sensors and cameras improves the accuracy of the gathered data.

Figure 13 shows a custom build drone that we used in this study. The technical specifications of this drone are presented in Table 1. The drone contains only the basic features to minimize manufacturing costs. We used this drone to obtain pictures on the bridge segments available at the Engineering Center campus of Florida International University. These bridge segments belonged to the exit ramp of the Fort Lauderdale airport, which were removed in 2013 because a new runway with different geometry was needed to be built. More details of the bridge segments can be found in Ref. [39]. The aerial view of the bridge obtained by the drone is available in Figure 14.

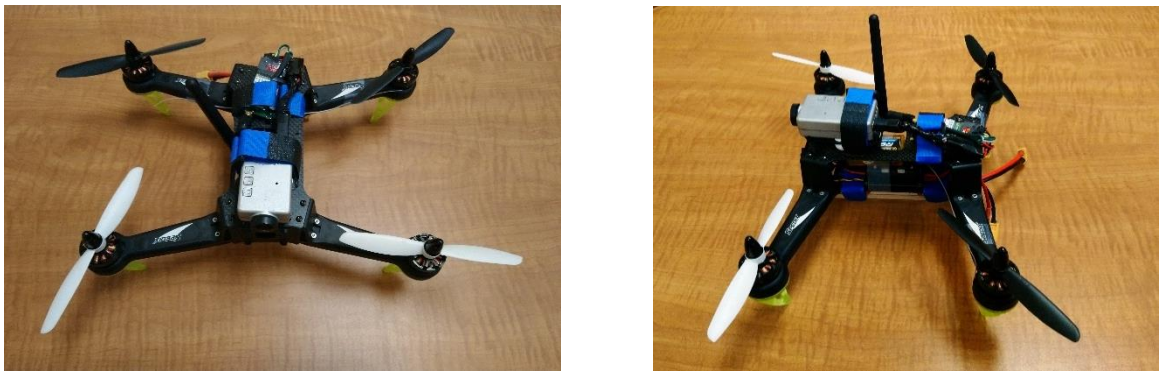

(a) (b)

Figure 13: Custom build drone; (a) front view, (b) side view.

Table 1: Custom build drone model for inspection.

Part	Model
Frame	Spedix S250Q Quadcopter Kit
Flight Controller	CC3D
Receiver	Orange R8DM DMSS
Camera	RunCam HD
Battery	Gens Ace 2200mAh 11.1V

Figure 14: Aerial view of the whole bridge segment.

Figure 15 shows the drone in operation. Although the weather condition was not much favorable and the wind and gust were affecting the drone stability, the pilot was able to control the drone and fly it very close to the bridge segments.

(a) (b)

Figure 15: View of the drone in operation (a) top corner and (b) bottom corner of the bridge segment.

A selection of the figures obtained by drone is illustrated in Figure 16. These figures present the possibility of obtaining detailed views of bridge condition using drones.

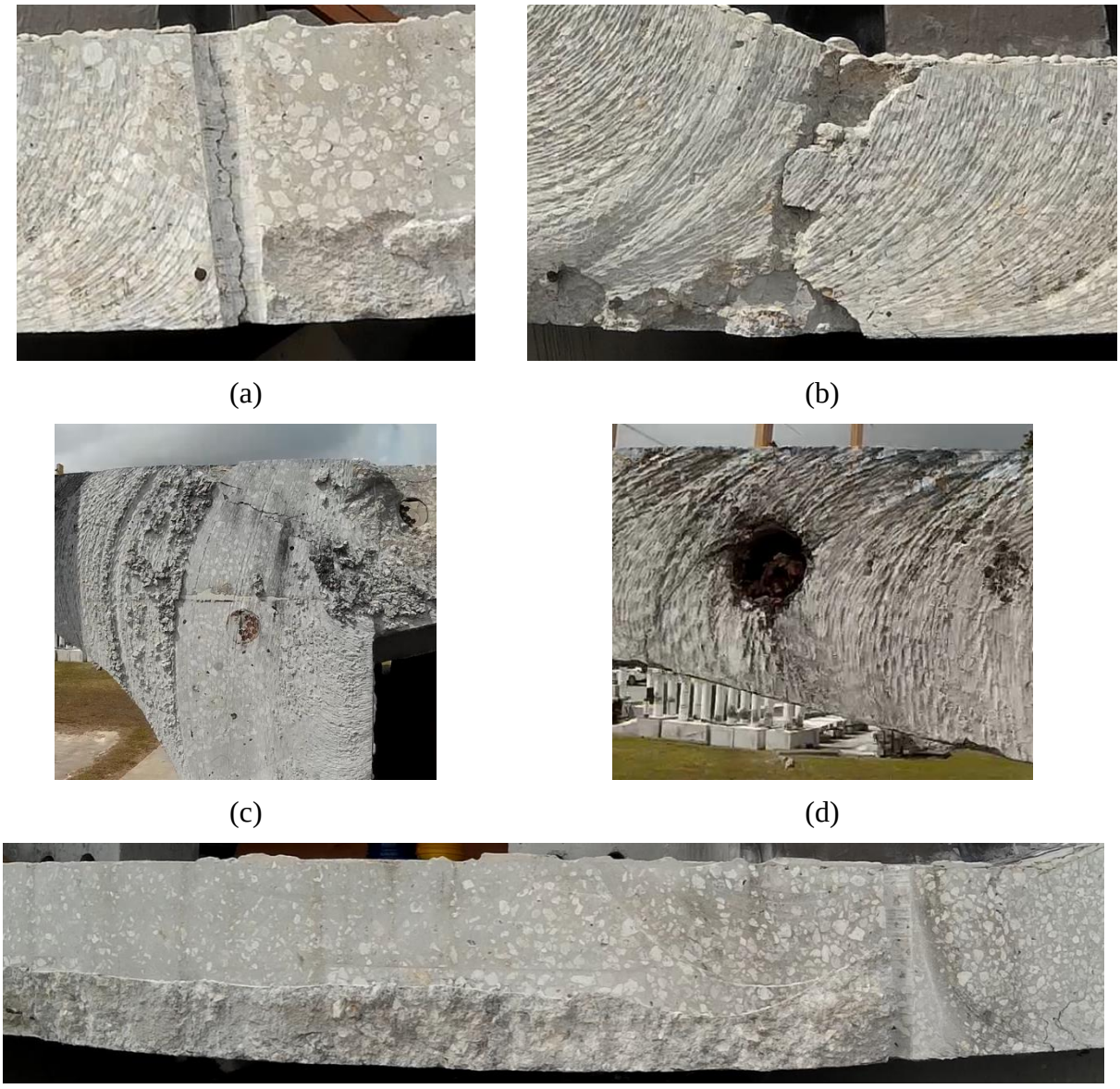

(a) (b)

(c) (d)

(f)

Figure 16: Inspection of the bridge obtained by custom build drone.

Furthermore, a thermal camera was used to obtain the same views that are presented in Figure 16 (a) and (b). The comparisons of these views, highlighting the cracks in bridge segments are presented in Figure 17. As mentioned, the thermal camera is one of the tools that can be easily incorporated into the drone due to its light weight. Thermal cameras detect the emitted infrared radiation from the object. If the material varies in the object, the temperature difference will be observable.

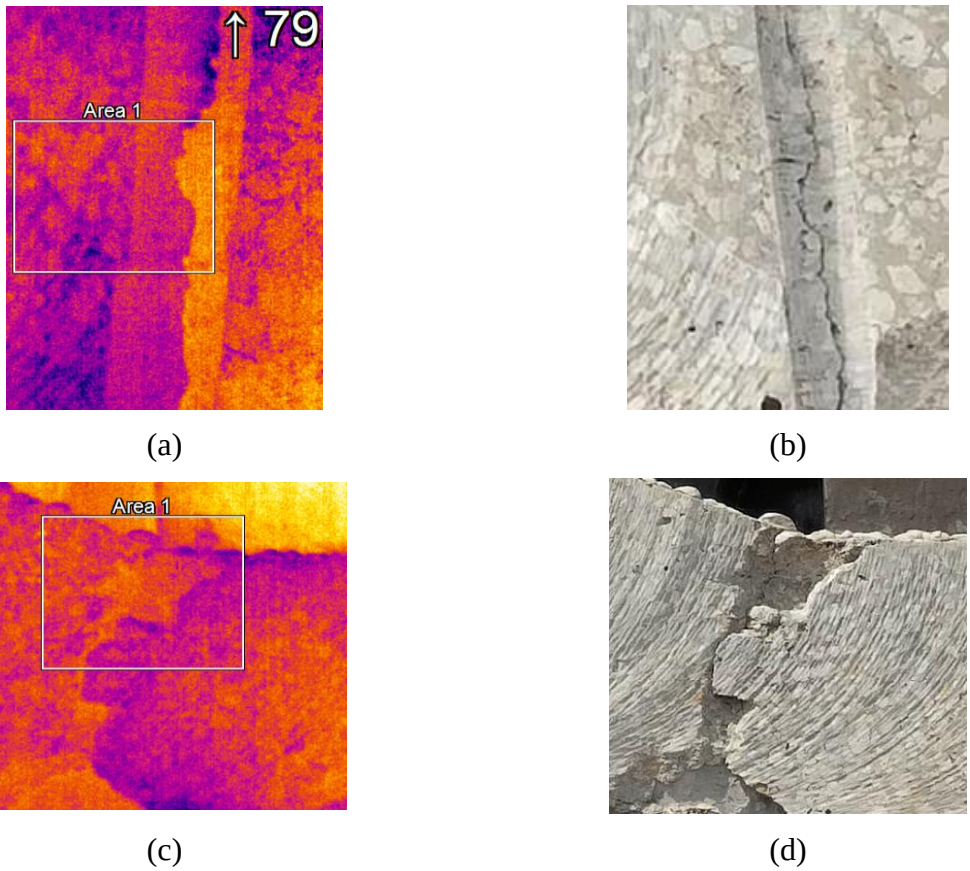

(a) (b)

(c) (d)

Figure 17: Comparisons of thermal pictures with regular pictures.

For further investigations and tests, a more advanced drone is required. If adequate funding is provided, one of the drones presented in Appendix B could be built or purchased. One of the main requirement of a suitable drone is the capacity of load that drone can carry. Drone with larger payload capacity can carry a regular and a thermal camera at the same time, which will result in more accurate ways of inspecting bridges. Additionally, more control systems such as proximity sensors or GPS can be added to the drone that makes the flight safer and smoother. Also, tools such as gimbal can be incorporated to keep the cameras stable and avoid transferring the vibration of the drone to the cameras.

CHAPTER 5. CONCLUSIONS AND RECOMMENDATIONS

UAVs have been part of many of today's human activities, from earth sciences to agriculture, entertainment, extreme weather observation, border and coastal patrol, sat-cell phone services, forest fire damage assessment, construction, military missions and many more. Due to different mission requirements, UAVs have been developed with a variety of configurations and capabilities. In this report, we presented an investigation on a different type of UAVs that are suitable for the construction and rehabilitation of bridges. Different design parameters were presented and explained in order to provide a path for DOT engineers in decision making on the configuration of a UAV with respect to its mission and stability.

UAVs can be used in many construction applications. Currently, most of these UAVs are rotorcrafts. These vehicles due to their vertical takeoff and landing and maneuverability characteristics are very suitable when the purpose is to obtain data in the vicinity of the object, i.e. bridge. In chapter 4, we presented two different rotorcraft drone, which we used to take tests on the stability of the vehicle with a mounted sensor and the other configuration for gathering images in close proximity of the structure. While these rotorcrafts are very suitable for the inspection services, they have some limitations as well. One of its major limitations is flying time. Due to the fact that the lift is generated primarily by the motors, it requires lots of power to maintain the flight, and this reduces the efficiency and the flight time of rotorcrafts.

On the other hand, fixed-wing UAVs uses the wing as the primary source of lift force production. As a result, they can fly for a longer duration of time with the same power source. However, these vehicles are not suitable when the mission requires flying in the vicinity of the bridge. They are more useful for the missions that require flying at higher altitudes, such as mapping. Another advantage of fixed-wing drones is gliding capabilities with no power. Also, fixed-wing UAVs can carry larger payloads for longer distances with less power, allowing to carry bigger sensors and more complicated sensors.

In chapter 4, we presented a very advanced numerical tool suitable for the stability analysis of the fixed-wing configuration. The input variables, different examples, and some linear and nonlinear aeroelastic analysis results were provided to show the ability of this computer program. One of the major advantageous of this code is the processing time, which is much faster than the available commercial codes. Also, any require sensor or camera can be simulated on the aircraft. In fact, it is imperative that DOT engineers examine the aeroelastic stability analysis in the presence of the sensors and camera, since any insignificant mass or payload can have significant effects on the aeroelastic stability of the aircraft. It should be pointed out that the referenced software and approach are applicable to fixed-wing aircrafts. Modifications and new developments are required for application of a similar software to rotorcrafts.

FUTURE WORKS

NATASHA is currently suitable for nonlinear aeroelastic trim and stability of fixed-wing aircraft, and it uses the 2D aerodynamic theory of Peters et al. [35]. To be able to analyze the rotorcraft configuration, NATASHA needs to be updated with different aerodynamic models. The aerodynamic analysis for the rotorcraft configurations is much more complicated than a fixed-wing one. "unlike the case of flow over a fixed wing which can often be analyzed by linear aerodynamics, the flow past a rotary wing is never what aerodynamicists consider to be "linear"." Also, there are different flight regimes that need to be considered. "First, there is hover, in which the thrust generated by the rotor blades just offsets the weight, and the helicopter remains stationary at some point off the ground. The second flight regime is vertical climb, in which additional thrust is required to move the helicopter upward. Third, there is vertical descent, a more complicated flight regime because of the presence of both upward and downward flow in the rotor disk which can induce significant blade vibration. Finally, there is the condition of forward flight, in which the rotor disk is tilted in the flight direction to create a thrust component in that direction. In forward flight, the component of the thrust in the forward flight direction must overcome the drag." [40]. Additionally, NATASHA assesses the stability of the fixed-wing aircraft by the *p*-method, which requires to be changed by another theory to be able to assess the stability of a rotorcraft configuration. One of the methods that are widely used for this purpose is the Floquet theory [41-43].

REFERENCES

[1] Kim, S. J., Lim, G. J., Cho, J., & Côté, M. J. (2017). Drone-aided healthcare services for patients with chronic diseases in rural areas. Journal of Intelligent & Robotic Systems, 88(1), 163-180.

[2] Koh, L. P., &Wich, S. A. (2012). Dawn of drone ecology: low-cost autonomous aerial vehicles for conservation. Tropical Conservation Science, 5(2), 121-132.

[3] Pobkrut, T., Eamsa-Ard, T., &Kerdcharoen, T. (2016, June). Sensor drone for aerial odor mapping for agriculture and security services. In 2016 13th International Conference on Electrical Engineering/Electronics, Computer, Telecommunications and Information Technology (ECTI-CON) (pp. 1-5). IEEE.

[4] Ventura, D., Bruno, M., Lasinio, G. J., Belluscio, A., &Ardizzone, G. (2016). A low-cost drone based application for identifying and mapping of coastal fish nursery grounds. Estuarine, Coastal and Shelf Science, 171, 85-98.

[5] Banu, T. P., Borlea, G. F., &Banu, C. (2016). The use of drones in forestry. Journal of Environmental Science and Engineering B, 5(11), 557-562.

[6] Restas, A. (2015). Drone applications for supporting disaster management. World Journal of Engineering and Technology, 3(03), 316.

[7] McNeil, B., & Snow, C. (2016). The truth about drones in mapping and surveying. Skylogic Res, 200, 1-6.

[8] Moser, V., Barišić, I., Rajle, D., &Dimter, S. (2016, January). Comparison of different survey methods data accuracy for road design and construction. In Proceedings of the International Conference on Road and Rail Infrastructure CETRA.

[9] Zink, J., & Lovelace, B. (2015). Unmanned aerial vehicle bridge inspection demonstration project (No. MN/RC 2015-40).

[10] Irizarry, J., & Costa, D. B. (2016). Exploratory study of potential applications of unmanned aerial systems for construction management tasks. Journal of Management in Engineering, 32(3), 05016001.

[11] Will Drones Transform Bridge Inspection? Roads and Bridges, September 6, 2016. https://www.roadsbridges.com/will-drones-transform-bridge-inspection

[12] Yang, C. H., Wen, M. C., Chen, Y. C., & Kang, S. C. (2015). An optimized unmanned aerial system for bridge inspection. In ISARC. Proceedings of the International Symposium on Automation and Robotics in Construction (Vol. 32, p. 1). IAARC Publications.

[13] Nazik Citir, Simon Laflamme, Katelyn Freeseman, Michael Scott, David Eisenmann, and Brent Phares (December 2018). INSPECTION AND QA/QC FOR ABC PROJECTS.

[14] Farhangdoust, S., Mehrabi, A., & Mosawi, S. S. (2018, March). NDT methods applicable to health monitoring of ABC closure joints. In 27th ASNT Research Symposium (pp. 75-87).

[15] Kalasapudi, V. S., Tang, P., Zhang, C., Diosdado, J., & Ganapathy, R. (2015). Adaptive 3D Imaging and Tolerance Analysis of Prefabricated Components for Accelerated Construction. Procedia engineering, 118, 1060-1067.

[16] Gundlach, J. (2012). Designing unmanned aircraft systems: a comprehensive approach. American Institute of Aeronautics and Astronautics.

[17] Austin, R. (2011). Unmanned aircraft systems: UAVS design, development and deployment (Vol. 54). John Wiley & Sons.

[18] Seo, J., Duque, L., & Wacker, J. P. (2018). Field Application of UAS-Based Bridge Inspection. Transportation Research Record, 2672(12), 72–81.

[19] Koch, C., Paal, S. G., Rashidi, A., Zhu, Z., König, M., &Brilakis, I. (2014). Achievements and challenges in machine vision-based inspection of large concrete structures. Advances in Structural Engineering, 17(3), 303-318.

[20] Unmanned Aerial Vehicle Bridge Inspection Demonstration Project, Final Report 2015-40, Office of Bridges and Structures, Minnesota Department of Transportation, July 2015.http://www.dot.state.mn.us/research/TS/2015/201540.pdf

[21] Will Drones Transform Bridge Inspection? Roads and Bridges, September 6, 2016. https://www.roadsbridges.com/will-drones-transform-bridge-inspection

[22] Metni, Najib, and Tarek Hamel. "A UAV for bridge inspection: Visual servoing control law with orientation limits." Automation in construction 17.1 (2007): 3-10.

[23] Murphy, Robin R., et al. "Robot-assisted bridge inspection." Journal of Intelligent & Robotic Systems 64.1 (2011): 77-95.

[24] Eschmann, C., Kuo, C. M., Kuo, C. H., &Boller, C. (2012, July). Unmanned aircraft systems for remote building inspection and monitoring. In Proceedings of the 6th European Workshop on Structural Health Monitoring, Dresden, Germany (Vol. 36).

[25] Zink, J., & Lovelace, B. (2015). Unmanned aerial vehicle bridge inspection demonstration project (No. MN/RC 2015-40).

[26] Chan, B., Guan, H., Jo, J., & Blumenstein, M. (2015). Towards UAV-based bridge inspection systems: A review and an application perspective. Structural Monitoring and Maintenance, 2(3), 283-300.

[27] Yang, C. H., Wen, M. C., Chen, Y. C., & Kang, S. C. (2015). An optimized unmanned aerial system for bridge inspection. In ISARC. Proceedings of the International Symposium on Automation and Robotics in Construction (Vol. 32, p. 1). IAARC Publications.

[28] Ellenberg, A., Kontsos, A., Moon, F., &Bartoli, I. (2016). Bridge related damage quantification using unmanned aerial vehicle imagery. Structural Control and Health Monitoring, 23(9), 1168-1179.

[29] Seo, J., Duque, L., & Wacker, J. (2018). Drone-enabled bridge inspection methodology and application. Automation in Construction, 94, 112-126.

[30] Wells, J. L., Lovelace, B., &Kalar, T. (2017). Use of unmanned aircraft systems for bridge inspections. Transportation Research Record, 2612(1), 60-66.

[31] Unmanned Aircraft Systems (UAS) https://www.faa.gov/uas/

[32] Hodges, D. H., & Pierce, G. A. (2011). Introduction to structural dynamics and aeroelasticity (Vol. 15). cambridge university press.

[33] Noll, T. E., Brown, J. M., Perez-Davis, M. E., Ishmael, S. D., Tiffany, G. C., & Gaier, M. (2004). Investigation of the Helios prototype aircraft mishap volume I mishap report. Downloaded on, 9, 2004.

[34] Hodges, D. H. (2003). Geometrically-Exact, Intrinsic Theory for Dynamics of Curved and Twisted Anisotropic Beams. AIAA J., 41, 1131 - 1137.

[35] Peters, D. A., Karunamoorthy, S., & Cao, W. M. (1995). Finite state induced flow models. I-Two-dimensional thin airfoil. Journal of Aircraft, 32(2), 313-322.

[36] Mardanpour, P., Izadpanahi, E., Rastkar, S., & Hodges, D. H. (2017). Effects of engine placement on nonlinear aeroelastic gust response of high-aspect-ratio wings. In AIAA Modeling and Simulation Technologies Conference (p. 0576).

[37] Mardanpour, P., Izadpanahi, E., Rastkar, S., & Hodges, D. H. (2017). Nonlinear aeroelastic gust suppression and engine placement. Journal of Aircraft, 54(6), 2402-2404.

[38] Izadpanahi, E., & Mardanpour, P. (2018). Nonlinear Aeroelastic Response of Highly Flexible Flying Wing Due to Different Gust Loads. In Nonlinear Systems-Modeling, Estimation, and Stability. IntechOpen.

[39] Azizinamini, A. (2017). Non-destructive testing (NDT) of a segmental concrete bridge scheduled for demolition, with a focus on condition assessment and corrosion detection of internal tendons.

[40] Conlisk, A. T. (1997). Modern helicopter aerodynamics. Annual review of fluid mechanics, 29(1), 515-567.

[41] Bauchau, O. A., & Wang, J. (2010). Efficient and robust approaches for rotorcraft stability analysis. Journal of the American Helicopter Society, 55(3), 32006-32006.

[42] Peters, D. A. (1994). Fast Floquet theory and trim for multi- bladed rotorcraft. Journal of the American Helicopter Society, 39(4), 82-89.

[43] Bauchau, O. A., & Nikishkov, Y. G. (2001). An implicit Floquet analysis for rotorcraft stability evaluation. Journal of the American Helicopter Society, 46(3), 200-209.

APPENDIX A: NATASHA MANUAL

A.1. Trim Input Variables:

It is assumed that all the input data is given in a consistent set of units and output results will be in the corresponding consistent units. Note that for the wing and other lifting surfaces, the elements are numbered from left to right (while standing behind the wing) and so are the nodes. For the fuselage and other slender bodies, the elements (and nodes) are numbered from the nose to the tail. For the lifting surface, the x-axis is thus along the beam going from left to right, the y-axis is pointed to the front of the wing and thus the z-axis is pointed up. For the slender body, the x-axis is thus pointing towards the tail, the y-axis points in the starboard direction, and z-axis is again pointing up. Element n is thus between node n and node n+1. To account for the fact that there is one additional node per beam, we have an unused element number at the end of each beam. Thus, for a two beam aircraft with five elements each, the first beam has elements 1-5 and nodes 1-6, and the second beam has elements 7-11 and nodes 7-12. Thus, element 6 is non existent and so is element 12.

Nb: (integer) number of beams

N: (Nb×1 integer) number of elements in each beam

btype: (Nb×1 integer) type of the beam (1 for lifting surface and 2 for slender body)

rho: (double) density of air

gg: (double) earth gravity

BC_flag0: (integer)

0 = full aircraft free-free case

1 = symmetric half aircraft case

2 = cantilevered wing case

ref_beam0: (integer) reference beam; ref_beam0 along with ref_node0 determine where the flight dynamic variables are specified and how we initialize certain variables at the beginning for prior_soln_flag = 2. It also has to be the first beam where variables are calculated in post processing and thus ref_beam0 = beam_conn(1,1). (For symmetric/cantilevered, the ref_beam0 and ref_node0 has to be the point where we constrain the motion.)

ref_node0: (integer) reference node; ref_node0 is where the flight dynamic variables are specified

Clr_ref0: (3×3 double matrix) the rotation matrix for that transforms the variables given on the right of the node ref_node0 of the beam ref_beam0 to the frame where the flight dynamic variables are defined (flight dynamic variables are defined using the x-axis towards starboard, y-axis towards nose and z-axis up)

For BC_flag = 2:

groot: (3×1 double vector) the unit vector at the root for cantilevered case in the direction of the gravity (this vector is defined left of the reference node)

Vroot: (3×1 double vector) Velocity vector at the root for cantilevered case

Omegaroot: (3×1 double vector) Angular velocity vector at the root for cantilevered case

no_cont: (integer=2) number of controls (See the description for cont_values)

cont_values: (no_cont×1 double vector) vector of values of control used to determine the trim state (Trim_flag = 0) or used as starting values (Trim_flag = 1 and prior_soln_flag ~= 2) or not at all (prior_soln_flag = 2 and the cont_values are specifed in the file along with the other variables)

Trim_flag: (integer) required for BC_flag = 0 or 1

0 = use the cont_values and calculate the velocities

1 = use the UU/phi and calculate the cont_values (presently only the first 2 controls are used to trim the aircraft speed and climb rate, the other controls can be specified)

For Trim_flag = 1:

UU: (double) the magnitude of aircraft forward velocity

phi: (double) the angle of flight (giving the rate of climb)

Analysis_flag: (integer) determines what analysis to do after calculating steady-state (default is 0 if not defined)

0 = calculate the eigenvalues

1 = calculate the gust response

2 = calculate the eigenvalues and the gust response

For Analysis_flag = 1 or 2:

gust_var_flag: (integer) determines variables for which the gust response is calculated

0 = all variables are retained

1 = all variables at a particular node are retained

2 = all variables of a particular physical quantity are retained

3 = only particular physical quantities at particular nodes are retained

For gust_var_flag = 1:

gust_node: (?×1 integer) node at which gust response is calculated

For gust_var_flag = 2:

gust_quantity: (?×2 integer) variable number and direction of the quantity for which the gust response is calculated. The variable number has to be an integer between 1 and 7 correponding to Fhat_l Fhat_r Mhat_l Mhat_r Vhat_r Omegahat_r ghat_r. The direction is an integer between 1 and 3 corresponding to the x y z.

For gust_var_flag = 3:

gust_variable: (?×3 integer) node number, variable number and direction of the variable for which gust response is to be calculated.

gust_freq: (?×1 double) frequencies at which gust response is to be calculated

prior_soln_flag: (integer) determines the starting solution guess for the Newton-Raphson solution technique

0 = start with everything zero (except ghat_l = [0; 0; -1])

1 = start with initial velocity and angle-of-attack and pitch

2 = start with the variable from a file

For prior_soln_flag = 1:

U_inf: (double) initial guess for the airspeed

alpha_inf: (double) initial guess for the angle of attack

pitch_inf: (double) initial guess for the pitch angle

For prior_soln_flag = 2:

soln_file: (string) file name of the file from which to load the initial guess of the variables

NR_auto_damp: (integer) flag determining the method for Newton-Raphson damping

0 = constant damping according to NR_damp

1 = automatic damping, damping increased 0, 50, 75, 87.5 etc till the residual (error) decreases

For NR_auto_damp = 0

NR_damp: (double) damping values for Newton-Raphson procedure, normally between 0 and 1 (0 = no damping).

For NR_auto_damp = 1

NR_max_half: (integer) maximum times the damping is increased to check whether the residual decreases for a given iteration

NR_maxiter: (integer) maximum number of Newton-Raphson iterations for convergence

NR_feps: (double) value of the norm of the residual for convergence

NR_xeps: (double) value of the norm of the change in solution at each iteration for convergence

unsteady_aero_flag: (integer)

0 = quasi-steady aero: wake inflow and apparent mass effects neglected

1 = unsteady aero

NN = sum(N) + Nb: (integer) is the total number of nodes

dl: (1×NN double matrix) length of each element. Even though you have only sum(N) number of elements the size of all the element properties are NN. Thus for a system of three beams and N = [4;5;6], the value of dl(5), dl(11) and dl(18) are not used. You may or may not define these values.

k: (3×NN double matrix) initial twist/curvature

R, S, T: (3×3×NN double matrices) components matrices of the cross-sectional flexibility matrix [R S; S’ T]

mu, xi, II: (1×NN double matrix, 3×NN double matrix, 3×3×NN double matrix) elements of the cross-sectional mass matrix (per unit span). mu is the mass (scalar), xi is the vector from the reference point to the center of mass and II is a moment of inertia matrix (about the reference point). The mass matrix is given by [mu*eye(3) –mu*tilde(xi); mu*tilde(xi) II].

muhat, xihat, IIhat: (1×NN double matrix, 3×NN double matrix, 3×3×NN double matrix) data on added nodal mass. Note that the data (xihat and IIhat) is given in the reference frame right of the node. For nodal properties are of the order of NN and each one is a used data.

Clrhat: (3×3×NN double matrix) rotation matrix specifying the nodal kink, x_l = Clrhat*x_r, where the subscript denotes (right and left of the node) the frame in which the measure numbers of the variable x is calculated.

fhat_T, mhat_T: (3×NN double matrices) the force and moment applied at a node. Normally it is the thrust force. Note that this force/moment is a follower force/moment and given is the reference frame right of the node.

Hhat_eng: (3×NN double matrix) The angular moment vector of the engine (again given in the reference frame right of the node)

cont_no_T: (1×NN integer matrix) the control number in charge of varying the corresponding thrust. The integers should in general be between 1 and no_cont+1. Note that if the cont_no_T is equal to no_cont+1 then we are not controlling that thrust (it is zero).

b: (1×NN double matrix) (represents R for slender body) for lifting surface it is the semichord, while for a slender body it is the radius of the crosssection.

y_ac: (1×NN double matrix) (represents dRdS for slender body) for the lifting surface it is the distance between the aerodynamic center (or the point at which the C_m_alpha is measured) and the reference line (positive for aerodynamic center ahead of beam reference axis), while for the slender body it is the rate of change of the radius of the cross-section.

C_a: (3×3×NN double matrix) the rotation matrix denoting the rotation between the structural frame and the aerodynamic frame x_{struc} = C_a*x_{aero}. This is required if the airfoil reference chord line (used to determine C_l_0) is different from the y axis or the fuselage reference line is different from the x-axis.

C_aero: (10×NN double matrix) for lifting surface, it has the aerodynamic coefficients of the airfoil [C_l_0; C_l_alpha; C_l_beta; C_d_0; C_d_alpha^2; C_d_beta^2; C_m_0; C_m_alpha; C_m_beta; C_pitch]. For slender body, it has the aerodynamic coefficients of the fuselage [0; C_l_alpha; C_d_f; C_d_p; 0; 0; 0; 0; 0; 0].

cont_no_beta: (1×NN integer matrix) control number in charge of the flap deflection for lifting surface (not used for the slender body).

bpod: (1×NN double matrix) semichord of the pod; set to zero if no pod at the node.

lpod: (1×NN double matrix) length of the pod; set to zero if no pod at the node.

ypod_ac: (1×NN double matrix) the distance between the aerodynamic center and the reference line (positive for aerodynamic center ahead of beam reference axis).

Cpod_a: (3×3×NN double matrix) the rotation matrix denoting the rotation between the structural frame and the aerodynamic frame. Note that the pods are assumed to be vertical.

Cpod_aero: (2×(N+1) double matrix) aerodynamic coefficients of the airfoil [C_l_alpha C_d_0]. The airfoil is assumed to be symmetric.

NBC: (integer) number of boundary conditions (usually Nb-1)

beam_conn: (Nb×2 integer matix) it has the connection information for the beams. The first column has the listing of all the beam in the order in which you what to evaluate the initialization and post-processing. And second column has the Boundary condition number to use. It is required that you start this evaluation at the ref_beam0. Thus beam_conn(1,1) = ref_beam0 and since it does not require a BC beam_conn(1,2) is not used (and normally set to 0).

BC_beam1: (NBC×1 integer matrix) the first beam involved in the connection. When you use this along with beam_conn for initialization, we require that values for BC_beam1 be already calculated.

BC_node1: (NBC×1 integer matrix) the node number of the first beam

BC_beam2: (NBC×1 integer matrix) the second beam involved in the connection. When you use this along with beam_conn for initialization, we require that values for BC_beam2 be the beam that the values are calculated for.

BC_node2: (NBC×1 integer matrix) the node number of the second beam

BC_C: (3×3×NBC double matrix) the rotation matrix to convert from the frame of first beam to the frame of the second

A.2. Time marching Input Variables:

The following variables are only used for time marching solution.

dt: (double) time step for time marching

Nt: (integer) number of time steps to take during time marching

time_algo: (double) number from 0.0 to 1.0 denoting backward (0.0) – central (0.5) – forward differencing (1.0). 1.0 will not work because of algebraic constraints. 0.5 is the ideal (2^{nd} order accuracy). A number just less than 0.5 (like 0.495) should give high frequency damping.

init_cond_flag: (integer) determines the initial condition (replaces prior_soln_flag used in nonlinear steady-state/linearization). Also Trim_flag and sideslip_flag is no longer needed

0 = start with everything zero (except ghat_l = [0; 0; -1])

1 = start with initial velocity and angle-of-attack and pitch

2 = start with the variable from a steady-state solution file (λ (downwash) = 0) or from a time-marching solution without λ

3 = start with the variables from a time-marching solution with λ

For init_cond_flag = 1:

U_inf: (double) initial condition for the airspeed

alpha_inf: (double) initial condition for the angle of attack

pitch_inf: (double) initial condition for the pitch angle

For prior_soln_flag = 2 or 3:

init_file: (string) file name of the file from which to load the initial condition of the variables

init_cont: (no_cont×1 double vector) control values used to get the initial condition (It very important that the init_file used to start time marching be based on the steady-state solution for the exact model and init_cont)

cont_values_time: (no_cont×Nt double vector) this is a prescribed control time history values.

gust_flag: (integer) flag determining if gust is present

0 = no gust

1 = gust present

For gust_flag = 1

gust_file: (string) file name of the file from which to load the gust data (gust_data variable)

gust_beams: (?×1 integer) beams on which gust acts (note the beams have to be lifting surfaces; there is no model for gust on slender body)

gust_file_flag: (integer) flag determining the kind of gust data in the file

0 = same gust for all the elements on all the beams, thus the gust_data variable will be (Nt+1+2*ncmax)×1

1 = same gust for all elements in a given beam but different for different beams, thus the gust_data variable will be (Nt+1+2*ncmax)×size(gust_beams,1)

2 = different gust on each element, thus the gust_data variable will be (Nt+1+2*ncmax)×NNg

APPENDIX B: ROTORCRAFT DRONE SUGGESTED CONFIGURATIONS

In order to safely use a drone in inspection and mapping without stopping the traffic, the aircraft should be tested for reliability and stability. Any malfunction of the drone could put the drivers at risk and also cause damages to drone system. The live preview video is very important because it helps the pilot conduct the drone safely through obstacles. Considering the advantages, limitations and risks of using drone for bridge inspection, here we have compiled a list of commercially available and also custom build drones under $3000 that are suitable for bridge construction and rehabilitation applications.

B.1. DJI Mavic 2 Enterprise Dual

DJI brand is a pioneer in drone industry being recognized by smart, reliable and safety drones. The model Mavic 2 Enterprise is designed for precise flight and inspections services. This model comes with a 4K camera and a thermal camera (640x360). Also, it includes a speaker, spotlight and a beacon. All of these three accessories are very useful for inspection services.

Pros

- Dual camera (thermal and 4K camera).
- Full HD video transmission.
- Omnidirectional obstacle avoidance (8 proximity sensors).
- Reliable (24 powerful specialized computers make sure the drone is flying safety).
- 2x optical zoom and 3x digital.
- Speaker, spotlight and beacon accessories included.
- Compact and foldable.

Cons

- Low range camera pitch angle (-90° to +35°)

B.2. Parrot Anafi 4K

Parrot is another very renowned brand in the drone industry, developing efficient and high-quality UAVs.

Pros

- High range camera pitch angle (-90 to +90 allowing to inspect object above the drone).
- HD video transmission.
- 2.4x digital zoom.
- Compact and foldable.

Cons

- No obstacle avoidance
- Very limited payload capability

B.3. Custom build drone

The main advantage of a custom build drone is that we can combine all the features suitable for bridge inspections. The proposed custom build drone is made from a carbon fiber frame. It contains obstacle avoidance technology and high range camera pitch angle. Furthermore, this drone could be updated and modified to carry different tools and sensors.

We considered 3 combinations of components to design a custom build drone. The first scenario is the cheapest one with the basics components only to perform a steady flight along with the bridge structure. The pros and cons of this case are as follow:

Pros

- High range camera pitch angle (-90 to +90 allowing to inspect object above the drone).
- Basic obstacle detection (6 sonar sensors measuring).
- Provide great learning and skills development to students during the design and build.
- Upgradable and easy to modify.
- High payload capability.

Cons

- Low-quality video preview.
- Is not possible to start/stop video recording remotely.
- Much time for design and testing is needed.
- Big and not foldable.

Table 2 shows the components and price estimation to build the drone (case 1).

Table 2: Custom Build drone (case 1) components and prices.

Component	Description	Price
Frame	Carbon Fiber	$ 150.00
Transmitter/receiver	FlySky i6S	$ 61.19
Motors	4x Racestar 2212 980KV	$ 28.99
Speed Controller	Racestar RS20Ax4	$ 22.99
Battery	Multistar 5200mah	$ 29.95
Flight controller	Pixhalk PX4 2.4.8	$ 56.90
Power Sensor	APM Power module	$ 6.11
OSD	MinimOSD	$ 10.19
Video transmitter	Immersion RC 600mW	$ 12.59

Screen with receiver	Skyzone HD02 40CH 5.8Ghz	$ 96.99
Sonar	GY-US42 I2C Pixhawk (6x)	$ 58.98
GPS	Radiolink M8N GPS Module	$ 22.99
Gimbal	2 axis Brushless Gimbal	$ 38.99
Shipping		$ 22.50
Total		**$ 619.36**

The second case has a video transmitter, makes it possible to broadcast HD image. Pros and cons of the second case are shown below. The final price could be seen in Table 3.

Pros

- High range camera pitch angle (-90 to +90 allowing to inspect object above the drone).
- Basic obstacle detection (6 sonar sensors measuring).
- HD video transmission.
- Provide great learning and skills development to students during the design and build.
- Upgradable and easy to modify.
- High payload capability.

Cons

- Is not possible to start/stop video recording remotely.
- Much time for design and testing is needed.
- Big and not foldable.

Table 3 shows the components and price estimation to build the drone (case 2).

Table 3: Custom build drone (case 2) components and prices.

Component	Description	Price
Frame	Carbon Fiber	$ 150.00
Transmitter/receiver	FlySky i6S	$ 61.19
Motors	4x Racestar 2212 980KV	$ 28.99
Speed Controller	Racestar RS20Ax4	$ 22.99
Battery	Multistar 5200mah	$ 29.95
Flight controller	Pixhalk PX4 2.4.8	$ 56.90

Power Sensor	APM Power module	$	6.11
OSD	MinimOSD	$	10.19
Video transmitter	ConnexProsight HD system	$	350.96
Screen with receiver	Skyzone HD02 40CH 5.8Ghz	$	96.99
Sonar	GY-US42 I2C Pixhawk (6x)	$	58.98
GPS	Radiolink M8N GPS Module	$	22.99
Gimbal	2 axis Brushless Gimbal	$	38.99
Shipping		$	22.50
Total		**$**	**957.73**

The third design takes advantage of the last generation full HD video transmitter and a built-in screen on the transmitter of the drone.

Pros

- Possibility of incorporating a thermal camera.
- High range camera pitch angle (-90 to +90 allowing to inspect object above the drone).
- Basic obstacle detection (6 sonar sensors measuring).
- Full HD video transmission.
- Provide great learning and skills development to students during the design and build.
- Upgradable and easy to modify.
- High payload capability.

Cons

- Much time for design and testing is needed.
- Big and not foldable.

Table 4 shows the components and price estimation to build the drone (case 3).

Table 4: Custom Build drone (case 3) components and prices.

Component	Description	Price
Frame	Carbon Fiber	$ 150.00
Motors	4x Racestar 2212 980KV	$ 28.99
Speed Controller	Racestar RS20Ax4	$ 22.99

Battery	Multistar 5200mah	$ 29.95
Flight controller	Pixhalk PX4 2.4.8	$ 56.90
GPS	Radiolink M8N GPS Module	$ 22.99
HD video transmitter	HereLink with telemetry	$ 827.00
Sonar	GY-US42 I2C Pixhawk (6x)	$ 58.98
Gimbal	2 axis Brushless Gimbal	$ 38.99
Shipping		$ 12.90
Total		$ 1,249.69

B.4. Model comparison

Table 5 presents the capabilities and limitation ns of all models.

Table 5: Model comparison.

Parameter	Custom build drone	DJI Mavic 2 Enterprise	Parriot Anafi 4K
Flight Time	20 min	22-24	20-22
Camera quality	3840 x 2160 12MP	4096×2160 12MP	4096×2160 21MP
Camera pitch angle	-90 to +90	-90 to +30	-90 to +90
Zoom	No	2x Optical/3x Digital	2.4x Digital
Obstacle detection	Yes	Yes, with avoidance	No
Real time video quality	480p@30fps to 1080p@30fps	1080p@30fps	720p@30fps
Carrying load capacity	1500g	910g	200g
Price	**$ 619.36** to **$1,249.69**	**$ 2,429.00**	**$ 899.00**